

Desirée Weiß, B.Eng.

Phase transformation of Ti-6Al-4V during cooling

MASTER'S THESIS

to achieve the university degree of

Diplom-Ingenieurin

Master's degree programme: Advanced Materials Science

submitted to

Graz University of Technology

Supervisor

Assoc.Prof. Dr.techn. Maria Cecilia Poletti

Institute of Materials Science, Joining and Forming

Co-supervisor

Ricardo Henrique Buzolin, Eng. Mestr.

AFFIDAVIT

I declare that I have authored this thesis independently, that I have not used other than the declared sources/resources, and that I have explicitly indicated all material which has been quoted either literally or by content from the sources used. The text document uploaded to TUGRAZonline is identical to the present master's thesis.

Date

Signature

Acknowledgements

Firstly, I would like to thank my supervisor Assoc.Prof. Dr.techn. Cecilia Poletti for offering the possibility to be part of this project as well as for her constant assistance and advice. I would also like to thank my co-supervisor Eng. Mestr. Ricardo Buzolin for sharing his comprehensive knowledge, for his patient guidance and for offering valuable encouragement.

Further, the Christian Doppler Forschungsgesellschaft is fostered in the frame of the D-1303000107/CD-Labor for Design of high-performance alloys by thermo-mechanical processing. Along with this, I would like to thank voestalpine Böhler Aerospace GmbH & Co KG in Kapfenberg for their cooperation and support.

Moreover, I would like to express my thanks to my colleagues of the IMAT Modelling and Simulation Team, who always provided their knowledge and help. I also would like to thank the laboratory staff and secretary's office for their persistent support. Special thanks go to my fellow students for their support and motivation.

Last but not least, I would like to thank my family and friends for their great support in all aspects throughout my entire studies. Especially, I want to thank Matthias for all of the patience, encouragement and motivation he provided me.

Abstract

During thermo-mechanical treatments, the cooling rate varies between surface and center areas, especially in large components. In the titanium alloy Ti-6Al-4V this cooling rate gradient can cause development of different microstructures. As the mechanical properties of this $\alpha+\beta$ titanium alloy, especially fatigue resistance, toughness and ductility, are strictly correlated with the microstructure a proper thermo-mechanical treatment is of great importance.

The aim of this work is to describe the growth kinetics during continuous cooling of allotriomorphic α along the prior β grain boundaries (α_{GB}) and of globular primary α (α_p) in Ti-6Al-4V with initial bimodal microstructure. Cylindrical samples are heat treated at two different holding temperatures in the $\alpha+\beta$ field, 930°C and 960°C, and five different cooling rates, 10, 30, 40, 100 and 300°C/min, in order to investigate the microstructural changes depending on the cooling rate. Light optical as well as scanning electron microscopy are used to reveal the growth of α_p and α_{GB} qualitatively and quantitatively. The volume fraction and size of α_p , as well as the thickness of α_{GB} are measured. Additionally, interrupted tests at different temperatures are conducted to determine the progress of growth of α_p and formation of lamellar secondary α (α_s) and α_{GB} during cooling.

The continuous cooling tests reveal that the size of α_p particles increases while its size distribution broadens with decreasing of the cooling rate. Area fractions of α_p decrease with increasing the cooling rate and increasing the holding temperature. Moreover, the lower the cooling rate, the thicker the plates of α_{GB} . However, for cooling rates lower than 10°C/min, the plates are difficult to distinguished from the α_p because of their comparable size and morphology.

The interrupted tests show similar behavior for low and high cooling rates at the beginning of the cooling. The α_p particles grow and the α_{GB} plates form mainly from the globular α_p along the prior β grain boundaries. With progress of cooling, low cooling rates result in pronounced growth of α_p and thickened plates of α_{GB} which are predominantly consumed by the growing α_p particles. For high cooling rates, α_{GB} forms distinctive plates at the β grain boundaries and the growth of α_p is not pronounced.

Kurzfassung

Während thermomechanischen Behandlungen, speziell von großen Bauteilen, variiert die Abkühlrate zwischen oberflächennahen und zentralen Bereichen. In der Titanlegierung Ti-6Al-4V kann dieser Unterschied in der Abkühlrate die Entwicklung verschiedener Gefüge verursachen. Da die mechanischen Eigenschaften dieser $\alpha+\beta$ -Titanlegierung, insbesondere die Ermüdungsbeständigkeit, Zähigkeit und Verformbarkeit, eng mit dem ausgebildeten Gefüge zusammenhängen, ist eine geeignete thermomechanische Behandlung von großer Bedeutung.

Ziel dieser Arbeit ist die Beschreibung der Wachstumskinetik von allotriomorphem α entlang der früheren β -Korngrenzen (α_{GB}) und globularem primärem α (α_p) in Ti-6Al-4V mit ursprünglichem bimodalem Gefüge während der kontinuierlichen Abkühlung. Dabei werden zylindrische Proben bei zwei verschiedenen Haltetemperaturen im $\alpha+\beta$ -Phasenbereich, 930°C und 960°C, und mit fünf verschiedenen Abkühlraten, 10, 30, 40, 100 und 300°C/min, wärmebehandelt, um die Gefügeänderungen in Abhängigkeit der Abkühlrate zu untersuchen. Licht- sowie Rasterelektronenmikroskopie werden verwendet, um das Wachstum von α_p und α_{GB} qualitativ und quantitativ zu bestimmen. Sowohl Volumenanteil und Größe der α_p -Phase als auch die α_{GB} -Dicke werden gemessen. Zusätzlich werden unterbrochene Tests zur Bestimmung des Fortschritts des α_p -Wachstums sowie der Bildung von lamellarem sekundärem α (α_s) und α_{GB} während des Abkühlens durchgeführt.

Die kontinuierlichen Abkühlversuche zeigen, dass die α_p -Partikelgröße zunimmt wobei sich deren Größenverteilung mit sinkender Abkühlrate verbreitert. Die Flächenanteile der α_p -Phase nehmen mit zunehmender Abkühlgeschwindigkeit und Erhöhung der Haltetemperatur ab. Je niedriger die Abkühlgeschwindigkeit ist, desto dicker sind die α_{GB} -Plättchen. Bei Kühlraten unter 10°C/min können die Plättchen jedoch aufgrund der vergleichbaren Größen und Morphologie schwer von den α_p -Partikeln unterschieden werden.

Die unterbrochenen Tests zeigen zu Beginn der Abkühlung ein ähnliches Verhalten für niedrige und hohe Abkühlraten. Die α_p -Partikel wachsen und die α_{GB} -Plättchen bilden sich hauptsächlich ausgehend von diesen entlang der früheren β -Korngrenzen. Mit fortschreitender Abkühlung führen niedrige Abkühlraten zu einem ausgeprägten Wachstum von α_p und verdickten α_{GB} -Plättchen, die vorwiegend von den wachsenden α_p -Teilchen konsumiert werden. Für hohe Abkühlraten bilden sich markante α_{GB} -Plättchen an den β -Korngrenzen während das Wachstum von α_p gering ist.

Contents

Affidavit.....	II
Acknowledgements	III
Abstract	IV
Kurzfassung.....	V
Contents	VI
1 Introduction.....	1
2 State of the art.....	2
2.1 Titanium and its alloys.....	2
2.2 $\alpha+\beta$ alloys.....	5
2.3 Ti-6Al-4V	8
2.3.1 $\beta \rightarrow \alpha_{GB}$ transformation.....	10
2.3.2 $\beta \rightarrow \alpha_s$ transformation	11
2.3.3 α_p growth.....	12
3 Methodology.....	15
3.1 Material and sample preparation	15
3.1.1 Batch A	15
3.1.2 Batch B	16
3.2 Dilatometry	17
3.2.1 Setup	17
3.2.2 Continuous cooling tests.....	20
3.2.3 Interrupted cooling tests	22
3.3 Microstructure investigation.....	23
3.3.1 Metallography	23
3.3.2 Microscopy.....	24
3.3.3 Inhomogeneity in batch A	25
3.3.4 Image analysis.....	27
3.3.5 Representation of measured data.....	30
3.3.6 EBSD measurements	30
3.4 Analysis of dilatometer curves.....	31

4	Results	33
4.1	As received material of batch A.....	33
4.1.1	Microstructure of forged part before heat treatment.....	34
4.1.2	Microstructure of forged part after heat treatment.....	36
4.2	Microstructural features	37
4.3	Data analysis of microstructural features	46
4.4	Dilatometer curves	49
4.5	Data analysis of dilatometer curves.....	51
5	Discussion.....	53
5.1	Behavior of Ti-6Al-4V during cooling	53
5.1.1	Dependence of final microstructure on cooling rate.....	53
5.1.2	Sequence of formation and growth	54
5.2	Limitations of image analysis.....	56
6	Summary & Conclusions	57
7	Outlook.....	59
	References	60
	List of figures	62
	List of tables	65
	List of symbols and abbreviations.....	66

1 Introduction

Titanium combines high specific mechanical properties such as strength, toughness, ductility and fatigue resistance as well as excellent corrosion resistance, which makes it a perfect material for engineering applications [1]. However, owing to an energy intensive extraction and processing, the costs are still high. Therefore, titanium and its alloys are predominantly only used for applications in which weight is a critical factor. Weight reduction is a critical point in the aerospace industry. Besides impacting the material costs, decreasing weight has a direct impact on the consumed energy during usage. Concurrent, high mechanical requirements have to be met in aerospace industry. Titanium alloys are found to be a suitable material for this requirement.

Ti-6Al-4V corresponds to 80% to 90% of titanium alloys used in aerospace industry [2]. This $\alpha+\beta$ alloy is in general the most widely used titanium alloy and is further used in the medicine for medical prostheses as well as in the automotive, marine and chemical industry [3]. The mechanical properties of Ti-6Al-4V are strictly influenced by the microstructure. Therefore, the design of a suitable thermo-mechanical treatment is of great importance to achieve the desired microstructure and consequently the required mechanical properties.

The present work aims to describe the growth kinetics of globular primary α (α_p) and allotriomorphic α along the prior β grain boundaries (α_{GB}) in the $\alpha+\beta$ alloy Ti-6Al-4V during continuous cooling. Both constituents, together with the lamellar secondary α (α_s) constitute the bimodal microstructure of the investigated material. Knowledge of the phase transformation kinetics during cooling enables the maintaining of required mechanical properties, such as fatigue resistance, toughness and ductility. Heat-treatments using a dilatometer and the following microstructure analysis with light optical and scanning electron microscopy are performed to investigate the phase transformation kinetics for titanium alloy Ti-6Al-4V during continuous cooling. The micrographs are analyzed and globular α_p particle size distributions, average area number density and phase fractions are obtained. Furthermore, shape factors like aspect ratio and circularity which give information on the growth behavior of the α_p particles are considered. The thickness of α_{GB} plates is also investigated dependent on the cooling rate. The relation between cooling rate and growth of α_p and α_{GB} is further investigated with interrupted heat treatments. Therefore, the formation sequence and the growth of the globular particles as well as the plates of α phase at the grain boundaries are investigated in detail.

2 State of the art

Depending on the elements used for alloying of titanium and the conducted heat treatment, different phases with different volume fractions and morphologies can be present in the material at room temperature. The alloying elements as well as the heat treatment can therefore be used to achieve an optimal balance of properties according to the application.

2.1 Titanium and its alloys

Titanium belongs to the family of transition metals. Its characteristic properties are low density, high strength and high corrosion resistance.

The ores for titanium production are rutile (TiO_2) and ilmenite (FeTiO_3). Metallic titanium is obtained from the ores by chlorination, reduction and purification [1]. Because of the high reactivity of titanium with oxygen, inert atmosphere or vacuum is needed during production of titanium. This, in combination with high energy and starting material costs, are the causes for the high price of metallic titanium. Nevertheless, the high affinity to oxygen has also a positive effect. As it causes the formation of a stable and adherent oxide layer on the surface, it is the reason for the good corrosion resistance of titanium. However, above 600°C the rapid diffusion of oxygen leads to an enhanced growth of the oxide layer and causes embrittlement [3].

At 882°C titanium undergoes an allotropic phase transformation. When heating to above the transition temperature, the hexagonal close-packed α phase transforms to the body-centered cubic β phase. By alloying, the allotropic phase transformation (β -transus) temperature can be influenced and can be either increased or the β phase can be stabilized down to room temperature. In dependence of their effect on the transition temperature, alloying elements can be classified as neutral, α - or β -stabilizing elements [3]. Figure 1 gives different alloying elements and shows their influence on phase diagrams of titanium alloys.

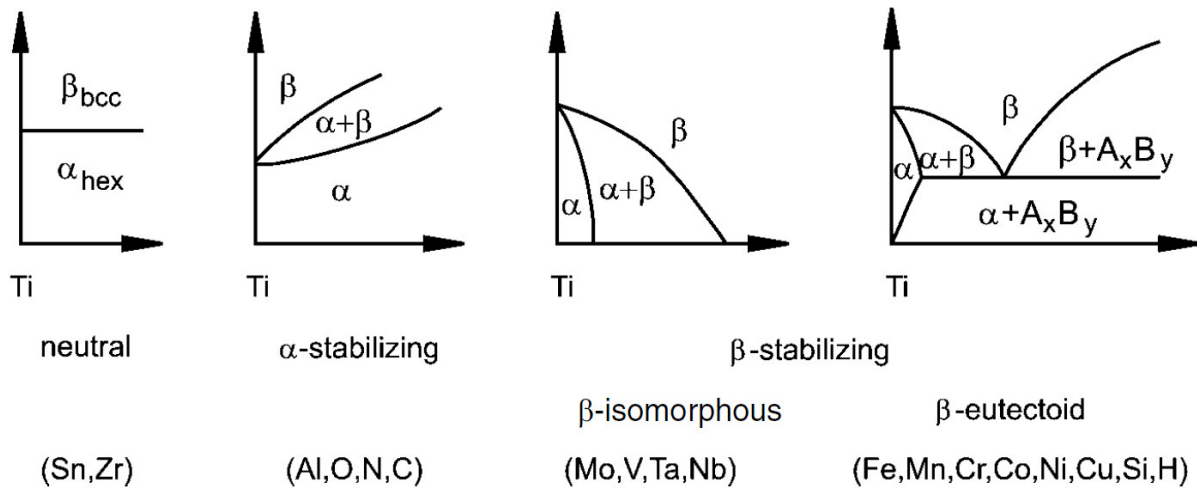


Figure 1: Schematic phase diagrams for Ti alloys showing the influence of alloying elements: neutral, α -stabilizing or β -stabilizing [4]

Titanium alloys can be classified into alpha (α), alpha-beta ($\alpha+\beta$) and beta (β) alloys with respect to the phases that exist in the material at room temperature [1]. Furthermore, the classes can be subdivided into near- α and metastable β alloys. The division can be described with a β -isomorphous phase diagram (Figure 2). Commercially pure titanium and alloys containing only α -stabilizing or neutral elements belong to the α alloys. Near- α alloys contain only a minor fraction of β -stabilizers whereas $\alpha+\beta$ alloys contain a higher amount of these elements. At the same time, the β volume fraction of $\alpha+\beta$ alloys is not exceeding a content of 5-40%. Although the name may suggest otherwise, near- α and α alloys do always contain a small amount of β phase. A higher fraction of β -stabilizers prevents the transformation of β phase to martensite upon fast quenching in metastable β alloys. Despite the higher fraction of β -stabilizing elements, the equilibrium α volume fraction of metastable β alloys can still reach more than 50%. [4]. The last group of titanium alloys, the β alloys, consist of only β phase.

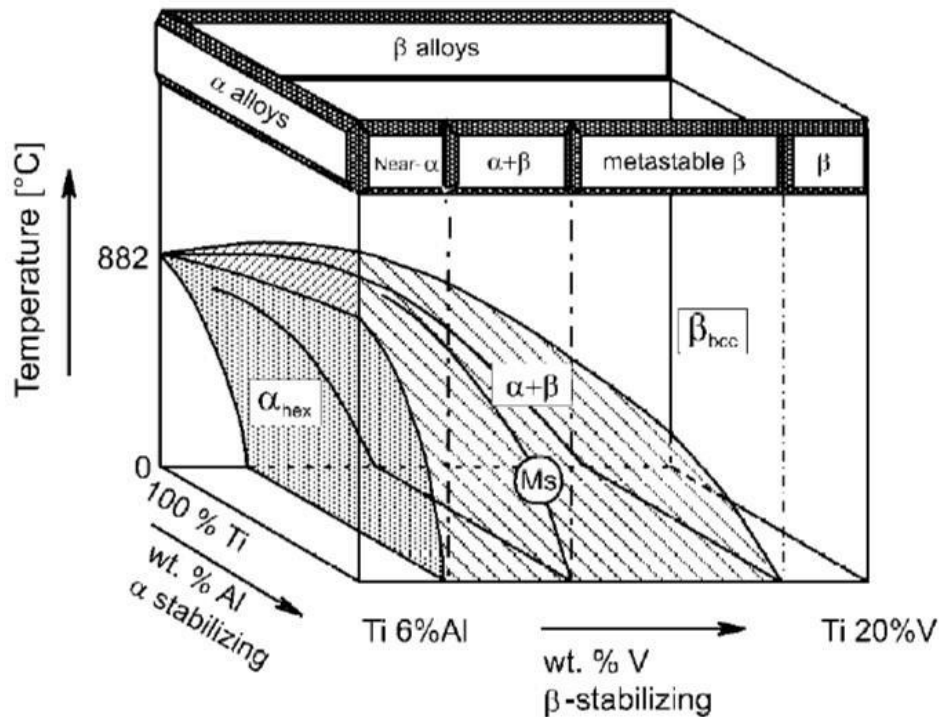


Figure 2: Classification of Ti alloys according to the three-dimensional β -isomorphous phase diagram [4]

During cooling, there are two possible mechanisms for the transformation of β phase to α phase. Depending on the cooling rate and alloy composition, the transformation can either occur martensitically or by diffusion controlled nucleation and growth. The martensitic transformation occurs during fast cooling and is the result of a shear type process, which causes the cooperative movement of atoms from the bcc lattice into the hexagonal lattice [3]. This transformation is a diffusionless process [4]. Different morphologies of martensite exist (cf. [3]) but will not be covered here as it is not the scope of this work.

The transformation by diffusion controlled nucleation and growth occurs for medium to low cooling rates which allow a sufficient diffusion of atoms. When cooling from the β phase field to the $\alpha+\beta$ field, the first observed transformation is the formation of α plates along the β grain boundaries. In this way, a nearly continuous layer of α phase is formed at the high-angle boundaries of the parent β phase. α phase with this morphology is also known as allotriomorphic α , referring to as α_{GB} . The plates itself are called grain boundary allotriomorphs [5]. During further cooling, plates of α phase form within the β grain. Parallel plates, which make up a so called α colony, either grow from the layer of α_{GB} or from the β grain boundary. Several colonies can form within one grain. The parallel plates making up one colony grow until they meet another colony which is referred to as sympathetic nucleation and growth. A microstructure consisting

of the parallel intragranular α plates and the retained β matrix is termed as lamellar [3]. The platelet morphology of α phase is named as secondary α (α_s) in this work. Figure 3 shows α_{GB} and α_s in a lamellar microstructure of Ti-6Al-4V. In optical micrographs, the α phase appears bright, while the β phase appears dark.

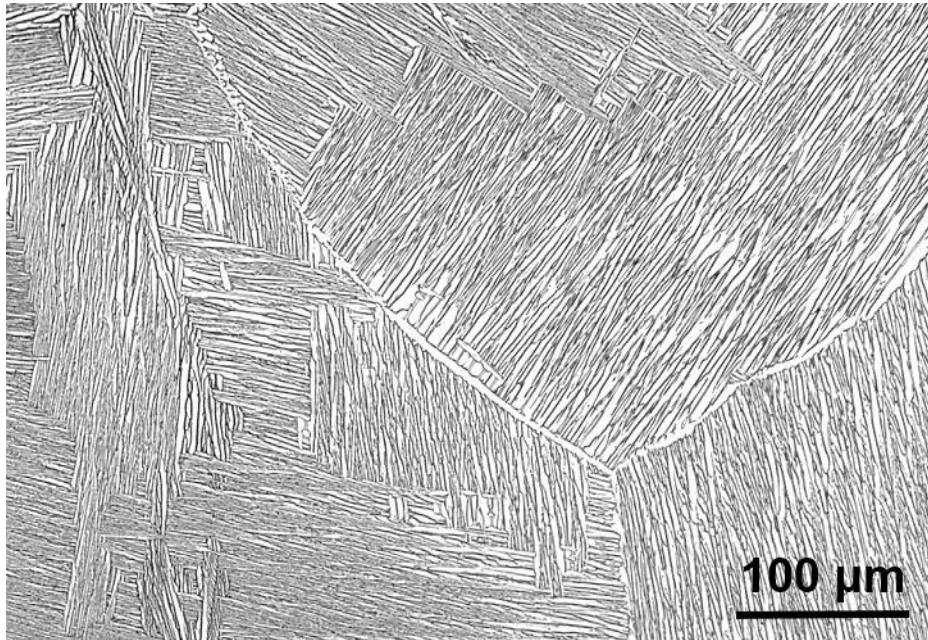


Figure 3: LOM micrograph of a lamellar microstructure of Ti-6Al-4V showing α_s colonies and allotriomorphic α_{GB} along the grain boundaries

2.2 $\alpha+\beta$ alloys

In general, $\alpha+\beta$ alloys can exhibit three different types of microstructures: fully lamellar, fully equiaxed and bi-modal structures (Figure 4). The bimodal microstructure is basically a mixture of equiaxed and lamellar one. It contains equiaxed primary α (α_p) in a lamellar $\alpha+\beta$ matrix [3]. For rapid quenching the lamellar $\alpha+\beta$ matrix is substituted by a martensitic needle-like microstructure.

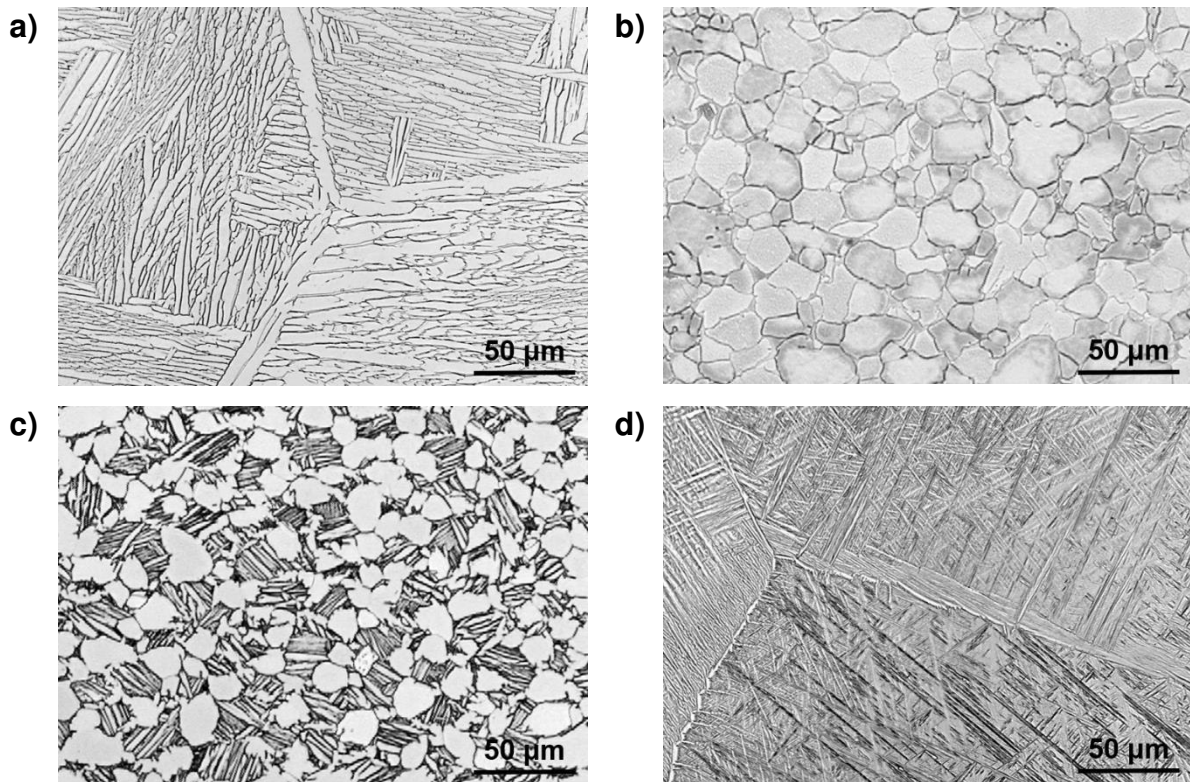


Figure 4: Different microstructures of $\alpha+\beta$ alloy Ti-6Al-4V: a) Fully lamellar, b) fully equiaxed, c) bimodal and d) martensitic structure

The different microstructures can be obtained by a suitable thermo-mechanical treatment. A fully lamellar microstructure can simply be achieved by a heat treatment in the β phase field and subsequent cooling with suitable cooling rate. During cooling, allotriomorphs will form first when temperature below T_{β} is reached. Afterwards lamellar α_s grows into the prior β grain. The intergranular α_s are coarse for very slow cooling. With increase in cooling rate, the plate thickness decreases and the colony size becomes smaller [3].

A deformation step is necessary to produce an equiaxed microstructure. In a first step, an alloy with lamellar microstructure has to be deformed plastically in the two-phase field to introduce enough dislocations to the material for full recrystallization of α and β phase in the next step [6]. The following step consists of a recrystallization treatment at a temperature in the $\alpha+\beta$ field which causes the formation of equiaxed, globular α particles. If the cooling is sufficiently slow or the temperature is low enough, the α_p grows extensively and only little intergranular layer of β phase is retained, originating a fully equiaxed microstructure. Intermediate cooling rates result in a reduced α_p growth and lead to a bimodal microstructure [3],[4].

By heating a bimodal microstructure to a temperature in the $\alpha+\beta$ field, the lamellar α_s dissolves and, when subsequent slow cooled, a fully equiaxed microstructure can be

obtained. On the contrary, a fully equiaxed microstructure can also be transformed into a bimodal one. This is achieved by a heat treatment in the $\alpha+\beta$ phase field followed by faster cooling [3]. It is important that the β transus temperature is not exceeded otherwise the primary α grains are dissolved and cooling from the β field results in formation of only α_s . As T_β is approached, the amount and size of α_p particles diminish [1].

The mechanical properties of a $\alpha+\beta$ alloy are dependent on the microstructure. When comparing lamellar and equiaxed morphology of α , both shapes show advantages for different fields of application. A lamellar morphology enhances fracture toughness and resistance to macrocrack propagation of the material. On the other hand, a globular morphology is more favored if an enhancement of ductility, low-cycle fatigue behavior and strength is of importance [1]. Consequently, a bimodal microstructure is often used to combine the advantages of both morphologies and create a balance of the required properties.

Table 1 provides a brief summary of some basic relations between the microstructure of a $\alpha+\beta$ alloy and its mechanical properties. If a change from the compared microstructure to the stated microstructure influences the property positively, it is designated as '+'. If the influence is negative, it is marked with '-'. As a result of this table, small α colonies and thin lamellas are always favored except for properties related to macrocrack propagation. Additionally, a small α_p particles size is of advantage except for resistance to macrocrack propagation and increase of creep strength. Moreover, a bimodal microstructure enhances yield stress, ductility and resistance to crack propagation of microcracks compared to a lamellar structure. The creep strain is minimal at intermediate cooling rates (100-500°C) for both fully lamellar and bimodal microstructures. Thus, the minimum in creep strain is referred to the microstructural feature existing in both microstructures and the creep strength for comparison of small and coarse α_s colonies and lamellae is marked with '+/-' in Table 1. [3]

Table 1: Qualitative correlation between some basic microstructure features and mechanical properties for $\alpha+\beta$ titanium alloys [3]

	Yield stress		Ductility		High cycle fatigue strength at 10^7 cycles		Resistance to fatigue crack propagation of microcracks		Resistance to macrocrack propagation and fracture toughness		Creep strength for strain of 0.2%	
Small α colonies / α lamellae compared to coarse lamellar structure	+	+	+	+	+	-	+/-					
Bi-modal structure compared to fully lamellar structure with same cooling rate	+	+	-	+	-	-						
Small α grain size compared to large α grain size of fully equiaxed structures	+	+	+	+	-	-						

2.3 Ti-6Al-4V

Ti-6Al-4V, also known as Ti64, is an $\alpha+\beta$ titanium alloys. The main alloying elements are Aluminum with ~ 6 wt.% and Vanadium with ~ 4 wt.%. As Aluminum is a α -stabilizing element, it strengthens the α phase. In addition, Vanadium as a β -stabilizer accounts for the retaining of the β phase down to room temperature [1]. Consequently, Ti-6Al-4V contains both the α as well as the β phase (Figure 5) and the microstructure can be controlled by thermo-mechanical processing to obtain fully lamellar, fully equiaxed, bi-modal or martensitic microstructures. In this way, a good combination of mechanical properties can be achieved by adapting a suitable heat treatment.

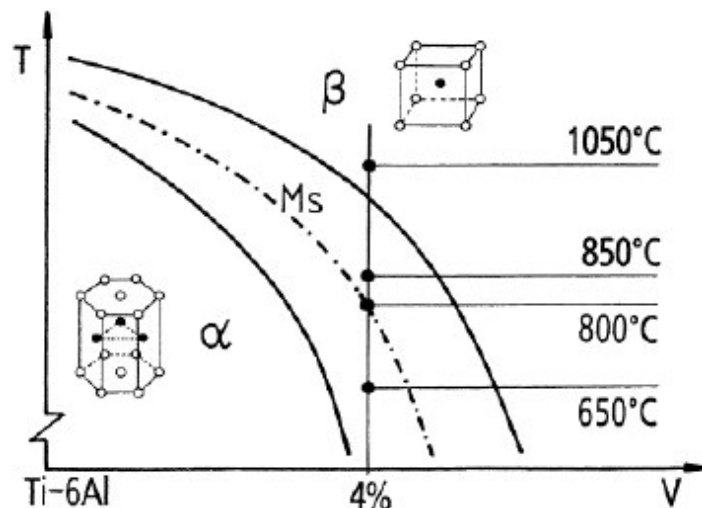


Figure 5: (Ti-6Al)-(V) phase diagram with straight line marking composition of Ti-6Al-4V [7]

Table 2: Typical mechanical properties of titanium alloy Ti-6Al-4V [4]

Alloy	T_{β} [°C]	Hardness [HV]	Elastic Modulus [GPa]	Yield strength [MPa]	Tensile strength [MPa]	Elongation at fracture [%]	Fracture toughness [MPa m ^{1/2}]
Ti-6Al-4V	995	300-400	110-140	800-1100	900-1200	13-16	33-110

Table 2 gives an overview of the range of values for the most important mechanical properties of Ti-6Al-4V. Because of the good balance of specific mechanical properties, high corrosion resistance and the comprehensive information that is available regarding its properties, this alloy is often used as structural material in aerospace industry [4]. Furthermore, the operating temperature of Ti-6Al-4V is superior to that of aluminum alloys which competes regarding the density. However, a maximum application of about 300°C limits the usage in the rotation section of aero-engines to the fan stage and some sections in the low pressure and high pressure compressor [3]. Further applications are in the medical sector as well as in the automotive, marine and chemical industries [8]. In the offshore oil and gas production, Ti-6Al-4V shows advantages compared to competing steel materials as it combines a low modulus of elasticity (50% of steel) with better seawater fatigue resistance [3]. The main target for the usage in automotive applications is the benefit of weight reduction. However, in most cases the use is restricted to racing and high-class vehicles due to the high material price [9], [10]. The application of Ti-6Al-4V in medicine ranges from hip and knee prostheses across trauma fixation devices like screws and plates to surgical instruments and artificial hearts [11].

The thermo-mechanical processing is decisive for the control of mechanical properties in $\alpha+\beta$ titanium alloys and therefore in Ti-6Al-4V. Throughout the whole processing route, the microstructure changes permanently. Considering a bi-modal starting microstructure, different phenomena occur during heat treatment in the $\alpha+\beta$ phase field. Heating dissolves the α phase. α_s dissolves first, followed by α_p and α_{GB} until phase fraction equilibrium is reached. Holding at a temperature in the $\alpha+\beta$ field can cause a coarsening of β grains and a decrease of α_p and α_{GB} phase fraction which stops when phase equilibrium is reached. With additional cold or hot working in the process, dislocations are produced in the material and a partial or full recrystallization can occur. When cooling from a temperature in the $\alpha+\beta$ field, either β phase transforms martensitically or globular α_p grows and allotriomorphic α_{GB} and secondary α_s form. These mechanisms are dependent on the cooling rate. In particular, the cooling rate

determines the size, shape and fraction of the different morphologies of the α phase and their temperatures of transformation and formation, respectively. In the following, this influence on alloy Ti-6Al-4V is explained based on the available literature.

2.3.1 $\beta \rightarrow \alpha_{GB}$ transformation

If Ti-6Al-4V is cooled from a temperature in the β phase field, the allotriomorphic α_{GB} starts to form prior to α_s . [12] For cooling from both, the β or $\alpha+\beta$ phase field, the α_{GB} formation and growth is dependent on the cooling rate. Pederson [12] described that for very slow cooling rates no α_{GB} is found decorating the grain boundaries when cooling from the two-phase field. The work of Semiatin et al. [13] confirmed this observation as they only found very little, occasionally amount of α at the grain boundaries for a cooling rate of 10°C/min from a temperature in the $\alpha+\beta$ field. On the contrary, the grain boundaries were noticeably decorated with a thin α layer for higher cooling rates of 42 and 194°C/min. Pederson [12] also mentioned visible amounts of α_{GB} for moderately fast cooling rates which allow a transformation of β phase into the platelet α_s phase. Furthermore, the amount and thickness of allotriomorphic α_{GB} decreased with increasing cooling rates.

Sun et al. [14] investigated the α_{GB} phase in the near- α alloy TA15 (Ti-6Al-2Zr-1Mo-1V) cooled from β phase field and found that the α_{GB} preferentially nucleated at triple junctions of the β grains and then grow to one side of the grain boundary forming a flat plate. Depending on the available energy and time for the growth, the allotriomorphic α may also grow from another triple junction or from the middle of one β grain boundary and thus forming an unconnected layer of α_{GB} . Moreover, the allotriomorphic α was divided into different morphologies: flat α_{GB} , zig-zag α_{GB} , and a mix of both (Figure 6).

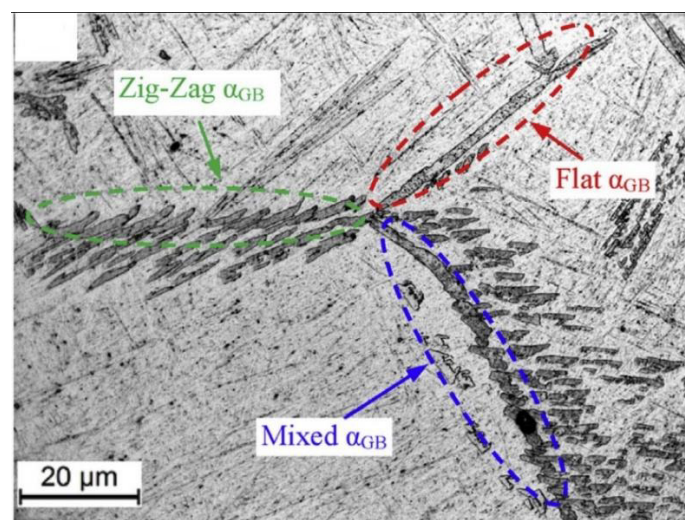


Figure 6: Micrograph of TA15 showing different morphologies (flat, zig-zag and mixed) of α_{GB} [14]

Figure 7 shows the evolution of allotriomorphic α for different vanadium contents in laser deposited compositionally graded alloy Ti-8Al-xV on one single β grain boundary conducted by Banerjee et al. [15]. The reduced impingement for increasing vanadium content cause the formation of discrete precipitates of α_{GB} at the grain boundary. For low vanadium contents a continuous layer formed.

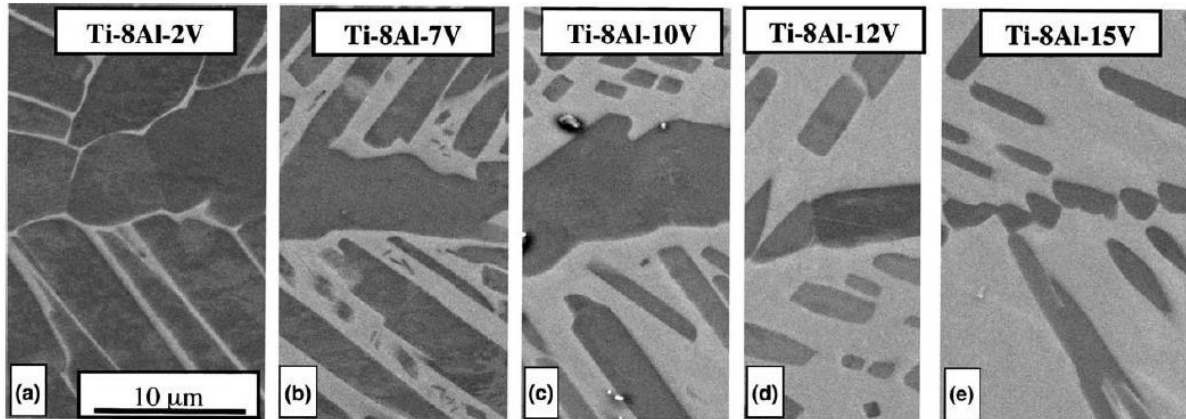


Figure 7: SEM-BS micrographs showing the influence of Vanadium content on the morphology of α_{GB} in titanium alloy Ti-8Al-xV [15]

2.3.2 $\beta \rightarrow \alpha_s$ transformation

Secondary platelet α forms within the β grain during cooling. Different possible starting points for the formation of the plates have been described [13], [16]–[19] (Figure 8):

- (A) Protuberances evolving from the α_p particles into the β matrix, which indicate a morphological instability.
- (B) Side plates extending from the α layer because of morphological instability
- (C) Homogeneous nucleation within the β grain due to high supersaturation in the β matrix

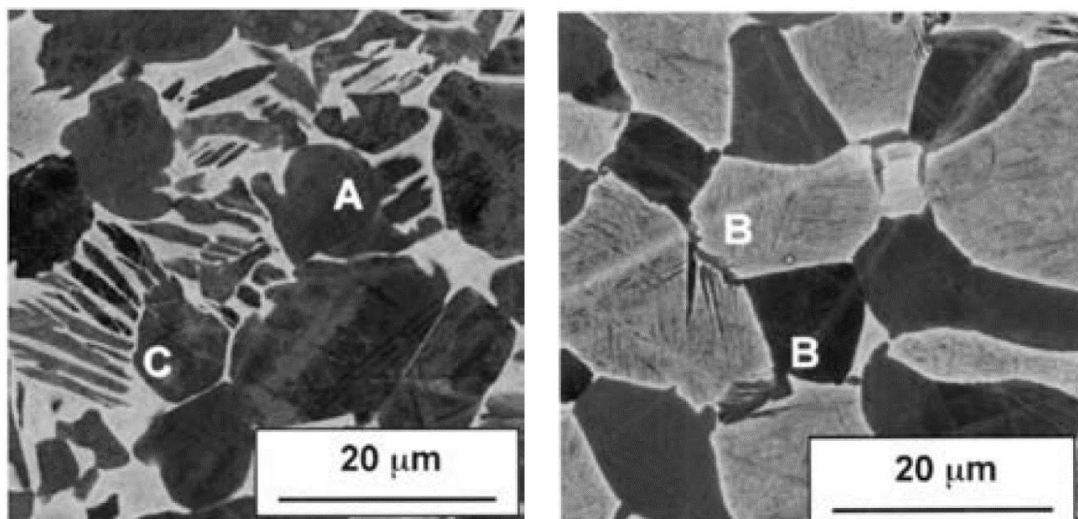


Figure 8: Micrographs illustrating the formation of α_s . Protuberances evolving from (A) α_p particles and (B) from α_{GB} layer as well as (C) nucleation within the β grain [13]

Several adjacent parallel plates form a α -colony. With a decrease in temperature the parallel plates grow into the grain until they meet other colonies. Semiatin et al. [13] observed, that during cooling from 870°C and 815°C at the rate of 42 and 194°C/min the measured volume fraction of α_s varied from β grain to β grain. This would have been expected for a diffusion process that started in one part of the grain and did not finish. Therefore, the variation is attributed as an effect of the sectioning. However, at 705°C all β grains contained α_s .

For very low cooling rates, only a insignificantly small amount of α_s is found in the β grains of the final microstructure of Ti-6Al-4V. [13] If the cooling rate increases, the nucleation rate of α_s and thereby the amount of α_s in the β matrix is enhanced. At sufficiently high cooling rates the nucleation of α_s plates occurs inside the prior β grains. Finally, when the cooling rate further increases, a martensitic transformation takes place. [12]

Furthermore, Semiatin et al. [13] observed that secondary α is formed at lower temperatures for higher cooling rates, which decreases the time for platelet thickening and leads to thinner plates. Conversely, an increased time, which is equal to longer diffusion periods, produces thicker plates. [20] The colony size decreases for higher cooling rates. Additionally, the maximum colony dimensions are limited to the β grain size. [12]

2.3.3 α_p growth

The growth of α_p is a diffusion-controlled process. For very slow cooling rates, the β phase is mainly transformed into α_p . The resulting microstructure consists almost entirely of large α_p particles. Small amounts of retained β phase can be found in between the particles. [12] Comparing the final microstructures, the amount of α_p is decreased for increasing cooling rates. [21] This was also observed for a near- α alloy TA15. Additionally, the investigations showed that the growth rate of α_p first increases for higher cooling rates and then decreases again at a certain cooling rate. [22]

Semiatin et al. [13] observed that α_p shows an epitaxial growth and that the growth is dependent on the diffusion of aluminum and vanadium in Ti-6Al-4V. Furthermore, the progress of growth at different temperatures during cooling was also shown. For the slowest cooling rate of 10°C/min, the α_p particles grew noticeably down to a temperature of 705°C. If cooling with 42°C/min, the substantial growth of particles stopped already between 870 and 815°C. Hence, the α_p growth stopped at higher temperatures for enhanced cooling rates.

Gao et al. [21] studied the epitaxial growth of globular α_p in Ti60 (in wt.%, 5.6Al, 3.8Sn, 3.2Zr, 0.5Mo, 0.4Nb, 1.0Ta, 0.35Si, 0.07C), which is a near- α titanium alloy. They observed the presence of rim- α phase, a phase surrounding the α_p particle, during cooling with low to intermediate cooling rates (Figure 9). The rim- α phase had the same crystallographic orientation as the interior of the α_p particle and thus, was considered as the evidence of epitaxial growth of primary α phase. Further analysis showed that the growth of α_p particles was mainly controlled by diffusion of aluminum and molybdenum. Extensions growing from α_p and preferentially along the β/β boundary were also investigated. The extending phase had the same crystallographic orientation as the α_p particle (Figure 10).

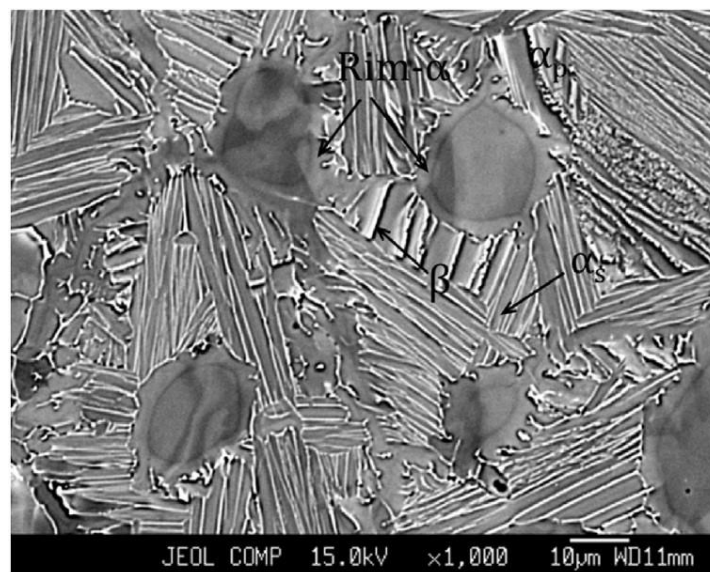


Figure 9: SEM-BSE micrograph showing rim- α phase in bimodal microstructure for a cooling rate of $90^\circ\text{C}/\text{min}$ [21]

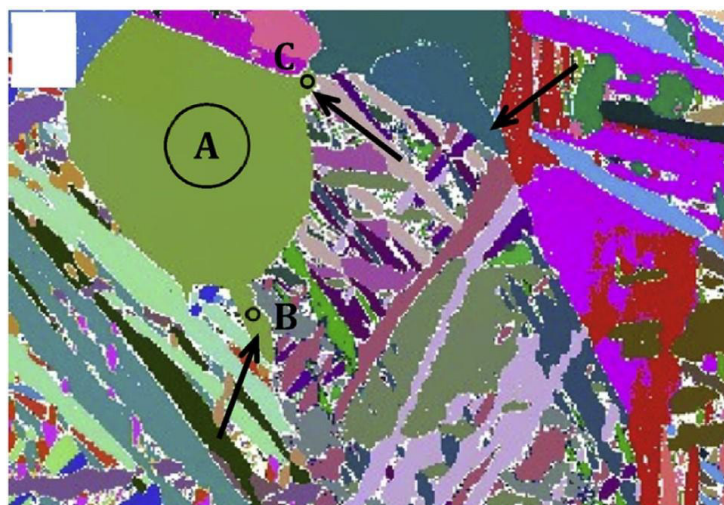


Figure 10: EBSD orientation map showing α_p particles and the extending phase (marked with black arrows) [21]

The retardation and finally the end of α_p growth can be attributed to two effects related to the formation of α_s : a pinning effect and the concomitant decrease in the matrix supersaturation, of which the second one is probably more important. The matrix supersaturation is the driving force for the growth of α_p , but it is also necessary for formation of α_s . In this way, the growth of α_p competes with precipitation of α_s when cooling with high cooling rates. Figure 11 shows how the evolution of volume fraction of α_p is affected by the formation of α_s plates. [13], [23]

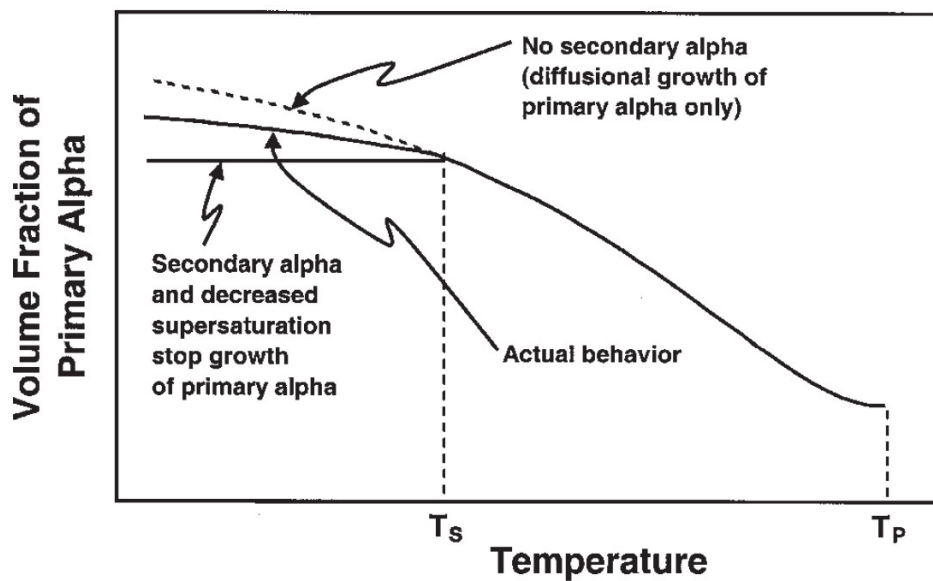


Figure 11: Effect of α_s formation on the volume fraction of α_p during continuous cooling (schematic) [13]

Meng et al. [24] complemented the work of Semiatin et al. [13] by considering two additional effects beside the diffusion-controlled growth by aluminum and vanadium redistribution and soft impingement, the overlap of diffusion fields of growing particles. [25] The effect of thermal history on the diffusion field around precipitates was implemented in the model.

3 Methodology

For the characterization of the phase transformation of β -phase into α_p , α_{GB} and α_s in Ti-6Al-4V during continuous cooling two sets of experiments were investigated. In the first set of heat treatments, the specimens were continuously cooled until room temperature so that the formed α_p and α_{GB} phases for different cooling rates were quantified. In the second set, the continuous cooling was interrupted at certain temperatures to investigate the phase transformation sequence for different cooling rates. Starting materials, sample preparation as well as the matrix of experiments are described in the following chapters. Furthermore, the analysis with light optical (LOM) and scanning electron (SEM) microscopies, subsequent image processing as well as evaluation of obtained dilatometer curves is explained.

3.1 Material and sample preparation

Titanium alloy Ti-6Al-4V samples from two batches were used for dilatometry. Batch A showed an inconsistent microstructure after heat treatment (chapter 4.1) and was therefore utilized to investigate qualitatively the influence of local microstructural and chemical inhomogeneity on the phase transformation. The batch B was utilized to obtain quantitatively the phase transformation kinetics for Ti-6Al-4V.

3.1.1 Batch A

A forged part with the chemical composition shown in Table 3 was investigated. The beta transus temperature (T_β) calculated with JMatPro[®] v.10 was 987.3°C. [26] JMatPro[®] is a software for simulation of material properties of several alloys. The calculations include phase equilibria as well as time temperature transformation diagrams and continuous cooling transformation diagrams. [27]

Table 3: Chemical composition of batch A [wt.%]

Element	Al	V	Fe	O	C	N	H	Y
Batch A	6.35	4.09	0.185	0.17	0.009	0.009	0.002	0.0025

Figure 12 shows the typical microstructure of the forged part. The bimodal microstructure has a α_p content of around 40-50%.

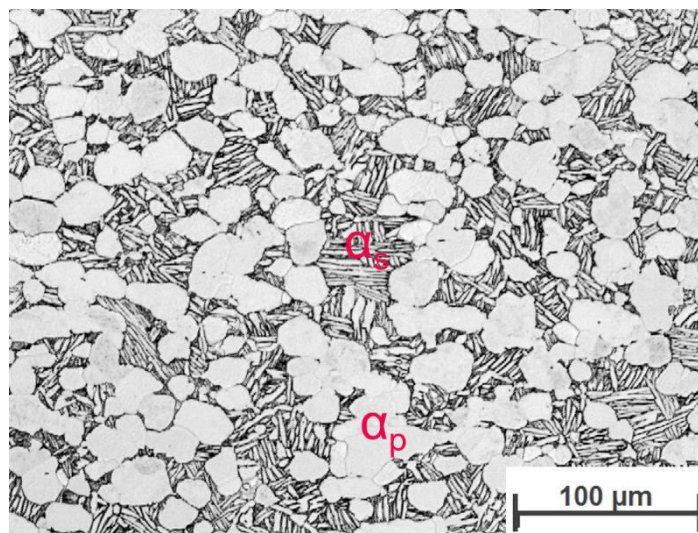


Figure 12: Light optical micrograph of the typical bimodal microstructure of the forged part from batch A

For the dilatometry tests, cylindrical samples were cut out of the forged part using wire eroding. After wire eroding, the samples were machined to their final cylindrical shape of diameter of 4-5 mm and length of 10 mm.

3.1.2 Batch B

Batch B used for the experiments of this work is namely batch 2 from the dissertation of P. Homporová [28] and Table 4 shows its chemical composition. The estimated β -transus is $\sim 1020^\circ\text{C}$. The alloy was cogged in different steps in β and $\alpha+\beta$ fields and annealed at 730°C for 1 hour followed by air cooling. [28]

Table 4: Chemical composition of batch B [wt.%] [28]

Element	Al	V	Fe	O	C	N	H	Y
Batch B	6.54	4.21	0.20	0.185	0.028	0.023	0.000335	<0.001

The typical microstructure of the as-received batch B is shown in Figure 13. In comparison with the as-received batch A, the microstructure of batch B contains a higher fraction of α_p with only little fraction of α_s . Cylindrical samples with a diameter of 5.5 mm and a length 10 mm were utilized for dilatometry.

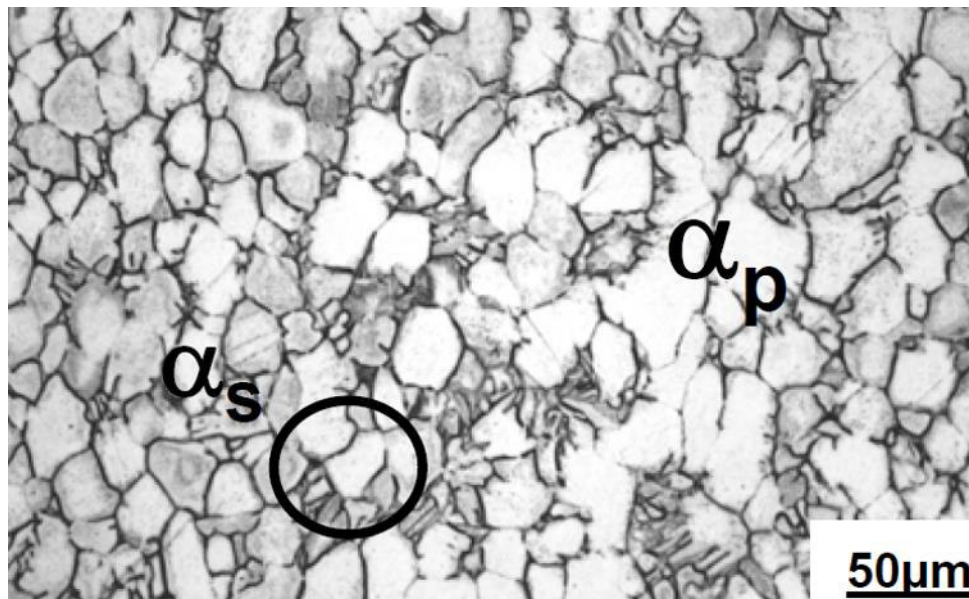


Figure 13: LOM micrograph showing the microstructure of batch B [28]

3.2 Dilatometry

The heat treatments performed to investigate phase transformation sequence and growth kinetics of α_p and α_{GB} phases during continuous cooling were performed using a dilatometer. Tests were carried out in a protective atmosphere of argon. An attached thermocouple to the surface of the sample was responsible for the temperature control during the test.

3.2.1 Setup

A dilatometer DIL 805A/D (TA Instruments, Hüllhorst, Germany) was used to perform the heat treatments of set 1, set 2 and set 3. The test chamber was evacuated and then flooded with argon. Tests including quenching were conducted by argon quenching.

For temperature control thermocouples were welded to the middle of the samples (Figure 14). Thermocouples of type K were used for samples of set 1, except for test 1_980_10 for which a S-thermocouple was used. Type K thermocouples consist of a nickel-chromium wire and a nickel-alumel wire and have a temperature range up to 1260°C. S-thermocouples combine a platinum rhodium wire and a platinum wire. The maximum operating temperature is up to 1600°C. [29]

During conducting of set 1, it was observed that K-thermocouples did mostly detach easily from the sample after heat treatment. Moreover, the K-thermocouples detached in some cases during heat treatment causing termination of the test. Those samples were not used for further investigation. The detaching after and during heat treatment rarely occurred when S-thermocouples were used. Nevertheless, the choice of the

thermocouple seemed not to be the reason for the microstructure reproducibility issues of set 1 (chapter 4.1), as all tests of set 1, except test 1_980_10, were conducted with a K-thermocouple. This assumption is supported by the fact, that test 1_980_10 was conducted with a S-thermocouple and also did not show a bimodal microstructure. Furthermore, the dilatometer stopped and showed an error message if the thermocouple was actually detached from the sample. Additionally, the power curves of the dilatometer were checked to find eventual power peaks, which would explain an exceeding of the set temperature caused by failure of the temperature control of the dilatometer. However, no distinctive peaks indicating a temperature overshooting were found in the power curves. Thus, the incorrect measurement of temperature leading to higher values because of the choice of thermocouple or by technical problems of the dilatometer was discharged as reason for inconsistent microstructure observed for samples of set 1.

Nevertheless, it was decided to use thermocouples of type S for further experiments (set 2 and 3) as the welding with the sample was better. Additionally, a second thermocouple was attached to the samples edge for set 2 and set 3 (Figure 15). The additional thermocouple enabled a reference measurement of the temperature, which let conclude if the heat treatment was performed as required. Moreover, the temperature gradient in the sample could be observed, which may have explained microstructural differences.

After welding the thermocouples, the sample was placed in the test chamber (Figure 15). The cylinder was clamped between two rods with minimum force and then moved into the induction coil (red arrow). The middle thermocouple was connected to a temperature controller, which turns the power on and off as needed.

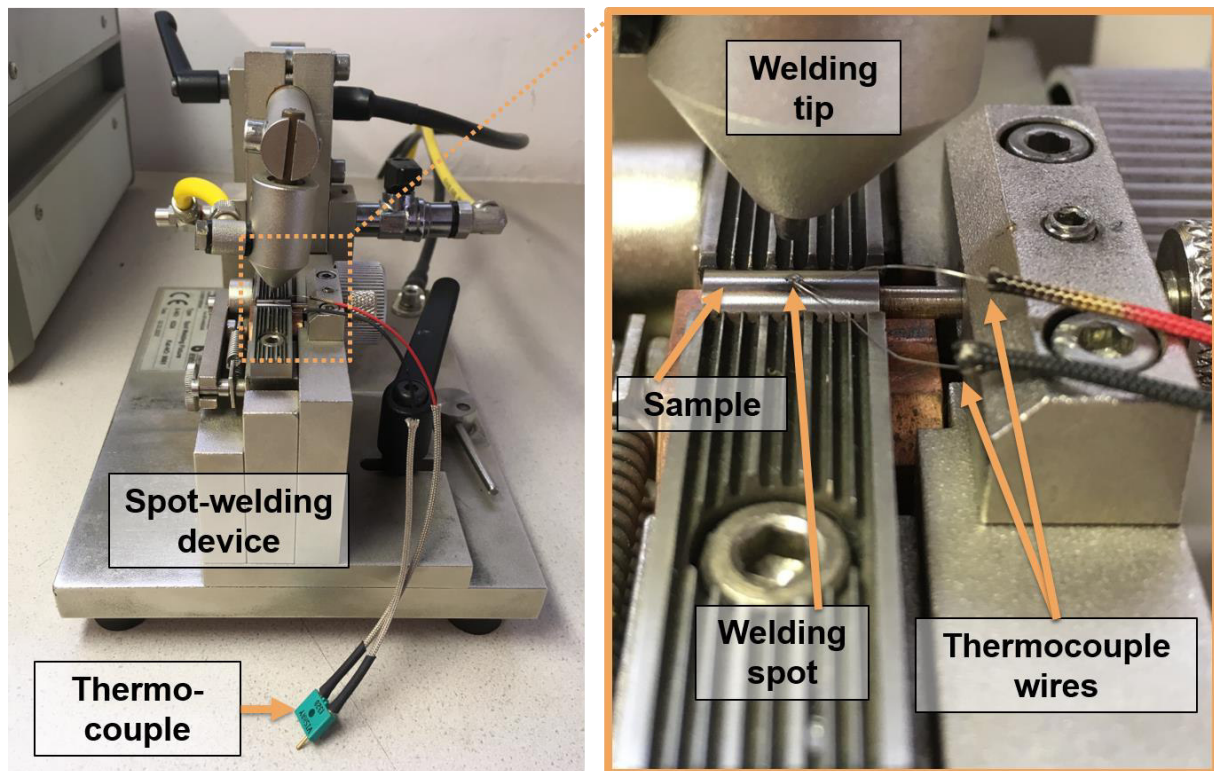


Figure 14: Welding of the thermocouple to the sample

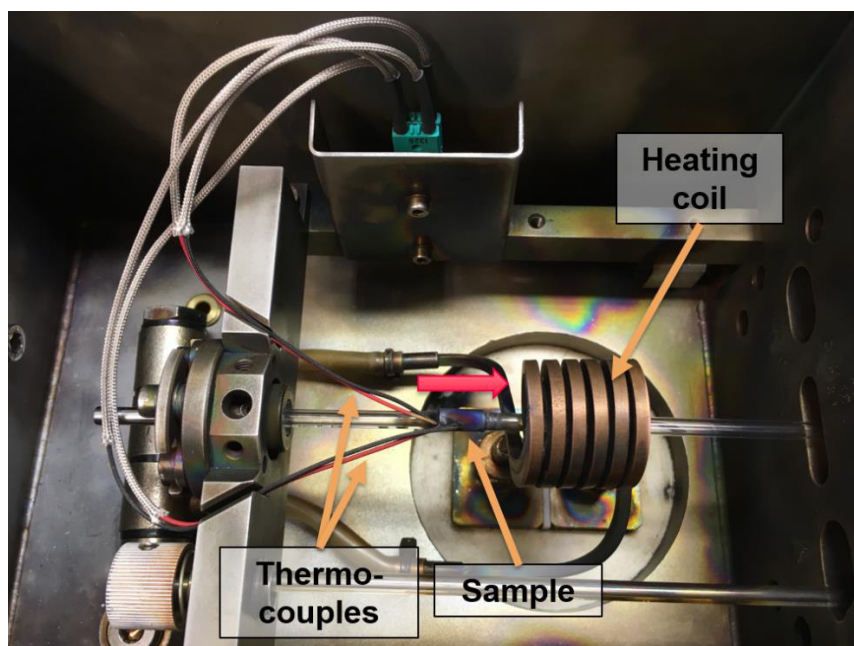


Figure 15: Placing sample in the sample chamber

No control/reference sample was available for the measurements. Therefore, the dilatometer curves could not be corrected with regard to instrumental errors. In consequence the reliability of the results of the analysis of the dilatometer curves is limited. They only show a rough qualitative tendency.

3.2.2 Continuous cooling tests

Aiming to investigate the formed morphologies of the α phase for different cooling rates, dilatometry tests with continuous cooling were performed. The fraction and morphological features of the formed α_p and α_{GB} phases were measured and its dependency on the cooling rate was established. A representation of the thermo-cycle performed for the continuous cooling tests is shown in Figure 16.

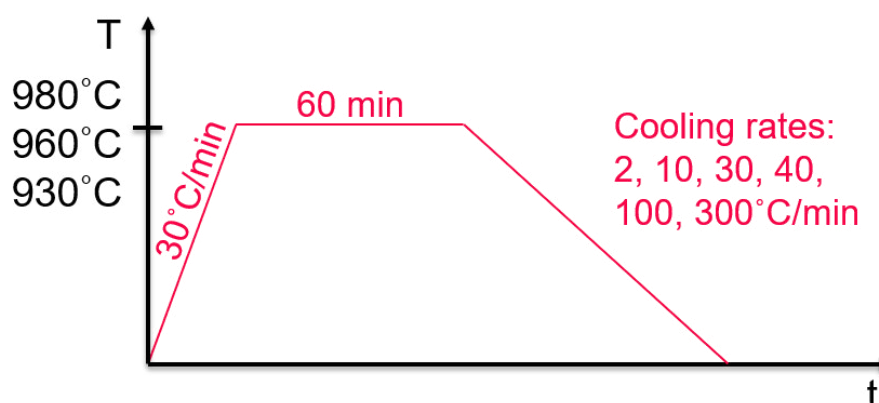


Figure 16: Representation of the temperature cycle utilized for the continuous cooling tests

After heating with a rate of 30°C/min, the samples were held for 60 min at three different holding temperatures in the $\alpha+\beta$ field, 930, 960 and 980°C, followed by continuous cooling until room temperature. The cooling was conducted with six different cooling rates: 2, 10, 30, 40, 100 and 300°C/min. The cooling rates were chosen so that the obtained microstructure at room temperature is bimodal.

The parameters for the performed tests are shown in Table 5. The samples from set 1 that were extracted from batch A exhibited inhomogeneity in the evolved microstructure. It seems that the β -transus was different for different regions of the batch A. Thus, incomparable microstructures were obtained after heat treatment. Therefore, the investigations performed for the set 1 aimed to evaluate the influence of local inhomogeneity on the phase evolution for the Ti-6Al-4V in hindsight. Batch B exhibited no microstructure inhomogeneity and set 2 was performed to evaluate quantitatively the phase evolution during cooling. However, some conditions were skipped for set 2 in comparison to the performed tests for set 1. Firstly, the fraction of primary α phase at 980°C is low, thus the volumetric number density is also very low. Consequently, the scatter for the quantification of the microstructure features (number density, are fraction and primary α size) is notable large. Therefore, 980°C was skipped for set 2. Furthermore, the cooling rate of 2°C/min was also skipped, as it leads to a fully globular microstructure. The aim of this work was to investigate the combined

growth of α_p , α_s and α_{GB} along the grain boundaries. The growth of primary α in a fully globular microstructure is out of the scope of this work. The parameters that were used for the set 2 (batch B) are also shown in Table 5.

Table 5: List of experiments and parameters for continuous cooling tests (set 1 & 2)

Set	Material	Test / Sample name	Holding temperature [°C]	Cooling rate [°C/min]
1	Batch A	1_930_2	930	2
		1_930_10		10
		1_930_30		30
		1_930_40		40
		1_930_100		100
		1_930_300		300
		1_960_2	960	2
		1_960_10		10
		1_960_30		30
		1_960_40		40
		1_960_100		100
		1_960_300		300
		1_980_2	980	2
		1_980_10		10
		1_980_30		30
		1_980_40		40
		1_980_100		100
		1_980_300		300
2	Batch B	3_930_10	930	10
		3_930_30		30
		3_930_40		40
		3_930_100		100
		3_930_300		300
		3_960_10	960	10
		3_960_30		30
		3_960_40		40
		3_960_100		100
		3_960_300		300

* valid for all experiments: heating rate 30°C/min, holding time 60 min

3.2.3 Interrupted cooling tests

In order to determine the transformation sequence of α_p , α_{GB} and α_s additional continuous cooling heat treatments interrupted at certain temperatures were carried out. The corresponding temperature cycle is shown in Figure 17.

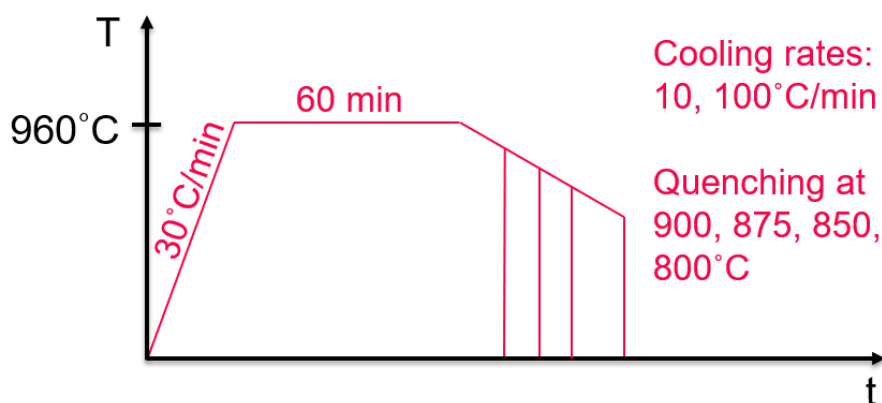


Figure 17: Temperature cycle for the interrupted continuous cooling heat treatments

After heating with 30°C/min to 960°C, the samples were held for 60 min at constant temperature. The subsequent cooling was performed with 10 and 100°C/min. To investigate the progress of the growth and formation of the different morphologies of α phase, the samples were quenched using Argon at four different temperatures, 900, 875, 850 and 800°C.

Because of the microstructure inhomogeneity of batch A, the interrupted continuous cooling heat treatments were only performed for batch B, designated as experiment set 3 (see Table 6). The frozen microstructure at 960°C was also investigated for comparison, and the sample is named 4_960_ArQ960. Additionally, a heat treatment was also performed above the β -transus (1080°C) aiming to investigate the growth of allotriomorphic α_{GB} separately. The sample is designated as 4_1080_100_ArQ875 and the parameters are listed in Table 6.

Table 6: List of experiments and parameters for the interrupted continuous cooling tests (set 3)

Set	Material	Test / Sample name	Holding temperature [°C]	Cooling rate until quenching starts [°C/min]	Interruption temperature [°C]
3	Batch B	4_960_ArQ960	960	-	960
		4_960_10_ArQ800		10	800
		4_960_10_ArQ850			850
		4_960_10_ArQ875			875
		4_960_10_ArQ900			900
		4_960_100_ArQ800			100
		4_960_100_ArQ850		850	
		4_960_100_ArQ875		875	
		4_960_100_ArQ900		900	
		4_1080_100_ArQ875	1080**	875	

* valid for all experiments: heating rate 30°C/min, holding time 60 min, quenching by flooding

with Argon

** holding time 20 min

3.3 Microstructure investigation

To enable the quantitative and qualitative analysis of the microstructure after heat treatment, the samples were metallographically prepared. In the present chapter this metallographic preparation as well as the following microscopic investigation and image analysis are described.

3.3.1 Metallography

In a first step, the heat treated cylindrical samples were ground by hand to produce a plane surface in longitudinal direction enabling a proper embedding. Then, the samples were hot embedded with the Struers® CitoPress-20 and the hot mounting resin PolyFast. Before starting with a systematic grinding procedure, the samples were ground using a Struers® Tegramin-30 until half of the sample diameter. All steps of the metallographic preparation are listed in detail in Table 7. After grinding with the silicon carbide grinding paper grit 2000, the samples were polished using OP-S (oxide polishing suspension). In the last step, the samples were cleaned and finally etched with the Krolls reagent, also listed in Table 7.

Table 7: Detailed steps and procedure for the metallographic preparation procedure of Ti-6Al-4V

Step	Abrasive	Suspension	Revolutions [rpm]	Force [N]	Time [min]	Description
Grinding	SiC #320	Water	-	-	-	To get plane surface for embedding.
Embedding	-	Polyfast	-	-	-	According to program.
Grinding to middle	SiC #180, SiC #320	Water	300	15	-	Until max. Cross-section is reached.
Grinding	SiC #320	Water	300	10	5	
	SiC #500	Water	300	10	5	
	SiC #800	Water	200	10	5	
	SiC #320	Water	200	10	5	
	SiC #1200	Water	300	10	5	
	SiC #1200	Water	300	5	5	
	SiC #2000	Water	300	5	5	
Polishing	MD-Chem	OP-S	40/ 150	20	10	Counter-rot.
	MD-Chem	OP-S	40/ 150	10	10	Counter-rot.
Step	Description					
Cleaning	<ol style="list-style-type: none"> Clean with wter and disp soap using your finger. Rinse with ethanol. Dry under hair dryer with cold air. 					
Etching	Etchant: Krolls Reagent - 91 ml distilled water - 6 ml HNO ₃ - 3 ml HF <ol style="list-style-type: none"> Immserse sample in etchant for 10-15 s and toss carefully. Rinse with distilled water and then under running water. Rinse with ethanol. Dry under hair dryer with cold air. 					

3.3.2 Microscopy

The metallographically prepared and etched samples were investigated using light optical (LOM) and scanning electron (SEM) microscopy. The LOM micrographs were used for the quantification of globular α_p particles. The micrographs were all taken from the center region of the sample, marked in Figure 18, to ensure that the analyzed region corresponds to the region where the thermocouples were welded during heat treatment.

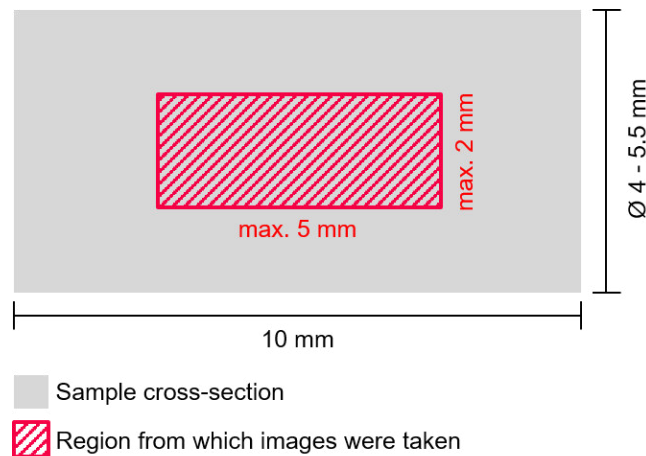


Figure 18: Schematic representation of the area investigated using light optical microscopy for the determination of the microstructure feature of the primary α phase

Micrographs were also obtained using the SEM to investigate in detail the features of the allotriomorphic α at the grain boundaries. The samples obtained from the continuous cooling interrupted heat treatments were also investigated using the SEM. Thus, the features of α_p , α_{GB} , and α_s could be investigated.

3.3.3 Inhomogeneity in batch A

The samples of set 1 were supposed to be heat treated in the $\alpha+\beta$ phase field. Thus, the originally bimodal microstructure should have been maintained. Only fraction, size and shape of the different α phases should have change dependent on the holding temperature and cooling rate. Nevertheless, half of the samples (Table 8) revealed a fully lamellar microstructure after heat treatment. This indicated that the heat treatment for these samples took place above the β -transus temperature.

As all samples heat treated at 980°C showed a microstructure without globular alpha and not a single sample heat treated at 930°C, this let conclude that the temperature during holding exceeded the β -transus temperature. The T_β can be exceeded during heat treatment either if the actual β -transus temperature of the material is in fact lower than the calculated one of 987.3°C or if the temperature control during heat treatment did not work properly and therefore the actual heat treatment temperature was higher than set.

Beside the samples heat treated at 980°C, half of the samples hold at 960°C also showed a non-bimodal microstructure. One possibility is that the temperature control was not accurate due to poor attachment of the controlling thermocouple. However, it can also lead to the assumption of having an inhomogeneous microstructure. In this case, the microstructure has to show a varying chemical composition that influences

locally the β -transus temperature. The fact that the second batch did not exhibit the same issue and reproducible results were observed lead to the conclusion that local variations of the chemical composition affected the β -transus temperature. Therefore, additional microstructure investigations were performed for the forged part of batch A described in the following.

Firstly, the surface of the forged part was grinded and polished as described in Table 7 and investigated using backscattered electrons (BSE) mode in SEM. The investigation showed slight differences in α_p fraction which indicated differences in the local chemical composition. Therefore, energy-dispersive X-ray spectroscopy (EDXS) was performed to check for changes in elemental composition. The revealed change in oxygen content was another indication for an inhomogeneous chemical composition. As oxygen is an α -stabilizing element, the β -transus temperature is raised if the oxygen content increases. But if the oxygen content decreases this, in fact, causes a lowering of T_β . The change in oxygen content could have been introduced during the wire eroding for sample cutting or even already during the casting, cogging or forging process. Besides oxygen, also other elements, which are not detectable with an EDXS analysis, could have caused a change in the β -transus temperature. These elements include nitrogen, carbon and hydrogen. Nitrogen and carbon are also α -stabilizers. In contrast, hydrogen is a β -stabilizing and can cause a significant decrease of the β -transus temperature. Qazi et al. [30] found that the β -transus in Ti-6Al-4V decreases from 1005°C to 815°C if changing the hydrogen content from 0 at.% to 30at.%, while the transformation temperature decreases rapidly between 0 at.% to 10 at.%. Moreover, the kinetics of the β -to- α transformation significantly slow down. Increasing hydrogen contents cause a shift of the nose temperature of the beginning of transformation to lower temperatures and also increase the nose time. Thus, martensite formation is already observed at slower cooling rates.

Secondly, macro etching of the prepared surface was performed to visualize segregations. In a first attempt, the previously polished surface was etched with a Keller reagent (95 ml distilled water, 2.5 ml nitric acid, 1.5 ml hydrochloric acid, 0.5 ml hydrofluoric acid). This etching only caused a micro etching and did not reveal any macroscopic segregations. In a second attempt an etching with a reagent, consisting of 10 ml hydrofluoric acid, 15 ml nitric acid and 75 ml distilled water, was performed. Again, the etching did not reveal any macroscopically visible inhomogeneity.

In a third step, a slice of 5 mm thickness was cut off the forged part. Then, the slice was heat treated in the oven in air for 10 min at 960°C and water quenched. Afterwards the slice was grinded, polished and etched using the Kroll's reagent to be investigated with light optical microscopy. The slight differences in α_p fraction observed in the first BSE-SEM investigation became more obvious after the heat treatment at 960°C for 10 min. This change is due to the increased dissolution of α phase for decreasing equilibrium fractions caused by different chemical compositions. It is probable that for longer heat treatment times, respectively longer homogenization times, the α_p in some regions would have been dissolved completely, as it was the case for some samples of set 1.

Summarizing, the variation of starting content of α_p in the forged part as well as the EDXS analysis indicated an inhomogeneous chemical composition of the produced part. Therefore, the samples of set 1 were not used for quantitative analysis of α_p and α_{GB} . As a consequence, set 1 was repeated as set 2 with material of batch B as well as set 3.

3.3.4 Image analysis

The globular particles were marked by hand in the LOM micrographs for the quantitative analysis of α_p . Five representative micrographs were analyzed for each cooling rate and holding temperature. The particles were marked manually using the software GIMP (GNU Image Manipulation Program). GIMP is an open-source software for image retouching and editing as well as free-form drawing. [31] The process is shown in Figure 19. Firstly, the edge of the particles was marked in black and then the area within the particle was filled with red color. Finally, the image was analyzed with ImageJ. ImageJ is an open source Java image processing program [32].

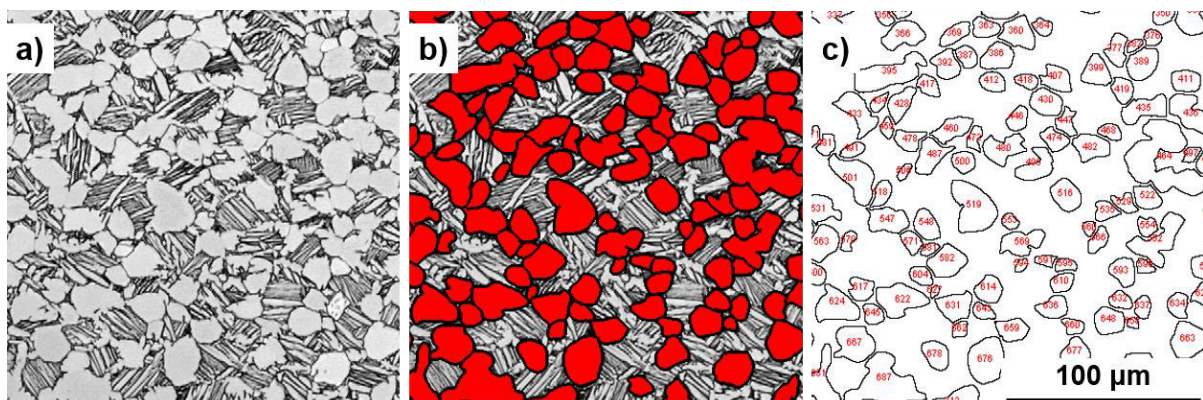


Figure 19: Methodology adopted for the quantitative analysis of α_p by a) light optical micrographs; marked globular α_p particles; and c) image analysis using ImageJ

The image analysis using ImageJ provides microstructure features such as individual particle area, perimeter, major and minor axis as well as the area fraction of α_p . Furthermore, shape descriptors like circularity (Equation 1) and aspect ratio (Equation 2) can be determined. Circularity describes the ratio of area and perimeter of a particle. If the circularity is one, the particle has the shape of a perfect circle. For lower values of circularity, the particle shape assumes either a flower or an elongated shape, which is schematically shown in Figure 20. The aspect ratio describes the relation between the major and minor axis of an ellipse that is fitted to the particle (Figure 21). The fitted ellipse has the same area, orientation and centroid as the original particle [33]. If the aspect ratio is equal to 1, the particle has the shape of a perfect circle. With increase of the aspect ratio, the shape changes more and more to a lamellar shape.

$$\text{Circularity} = 4\pi * \frac{[\text{Area}]}{[\text{Perimeter}]^2} \quad (\text{Equation 1})$$

$$\text{Aspect ratio} = \frac{[\text{Major Axis}]}{[\text{Minor Axis}]} \quad (\text{Equation 2})$$

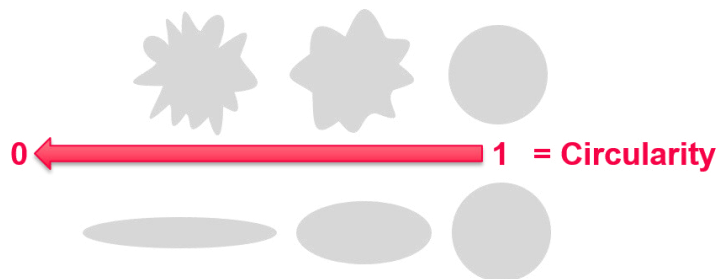


Figure 20: Schematic representation of the shape evolution of a particle with change in circularity value

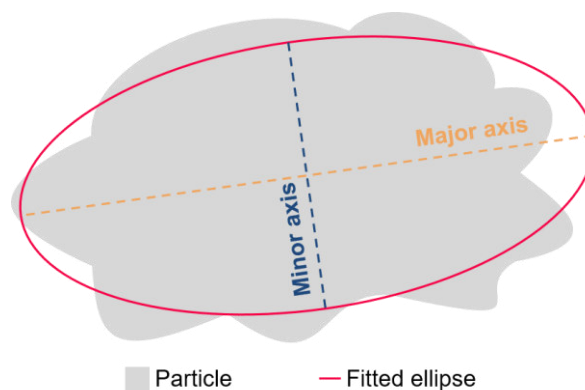


Figure 21: Schematics representation of minor and major axis of an ellipse that was fitted to a particle

A correction of the results obtained for the α_p fraction and diameter was performed as an issue related to the marking of the α_p was identified. During marking, the borders of the α_p particles, i.e. the grain boundaries, were marked with a line of a thickness of 3 pixels corresponding to 1.62 μm . Marking with a thinner line was not possible due to limitations of the ImageJ routine for measuring the properties of the marked particles. As the maximum average particle diameter is $\sim 18 \mu\text{m}$, 1.6 μm is comparatively large. This has considerably influence on the results for the α_p diameter. Moreover, the α_p fraction is reduced as the lines for marking cover up to 25% of the area of the micrographs. Based on this, a correction of the values for α_p fraction and diameter was performed. For correction of the diameter, 1.62 μm were added to the measured diameter. For correction of the α_p area fraction, the area fraction of the lines for marking was measured and half of this value was added to the area fraction of α_p . The corrected results are shown in chapter 4.3.

The SEM micrographs were used for the quantitative analysis of the α_{GB} . As shown in Figure 22 by the dashed lines, the thickness of the plates was measured by hand in regular distances. The measurement was performed using ImageJ.

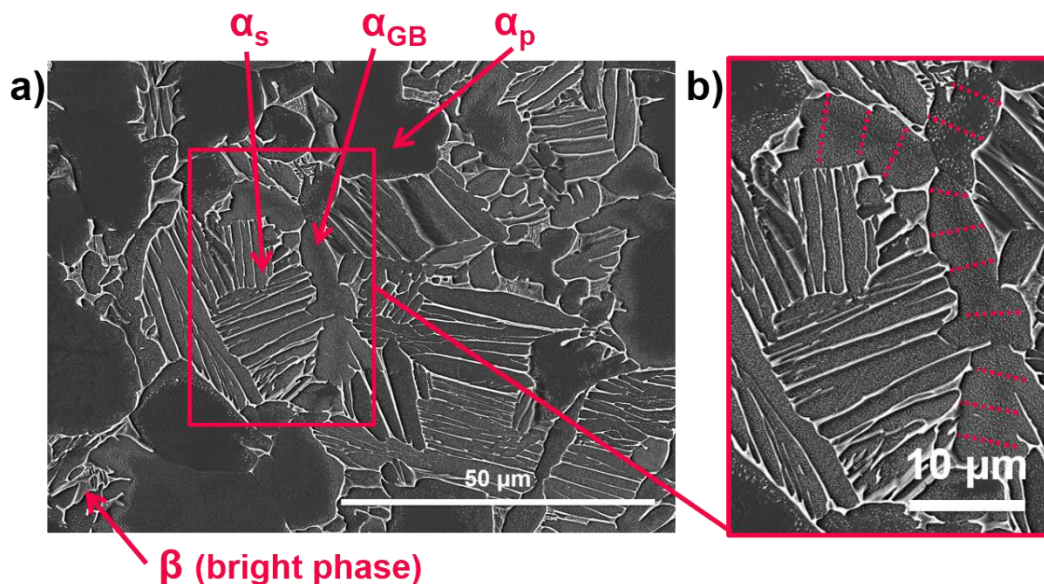


Figure 22: SEM-SE micrographs of bimodal heat treated Ti-6Al-4V. a) The different morphologies (globular, lamellar, plates at grain boundaries) of α phase are shown; b) highlight of an allotriomorphic α phase along the grain boundary with the dashed lines used for the measurements of the thickness of α_{GB}

3.3.5 Representation of measured data

The diameter of the measured primary α was represented in histograms for the different cooling rates using Origin[®] v9.0 [34], as schematically shown in Figure 23a. The counts were normalized by the total number of counts, so that the results for different cooling rates are comparable. In the last step, a function was used to fit the histogram enabling a better representation of the distributions for the investigated cooling rates (Figure 23b). Similar procedure was adopted for the circularity and aspect ratio.

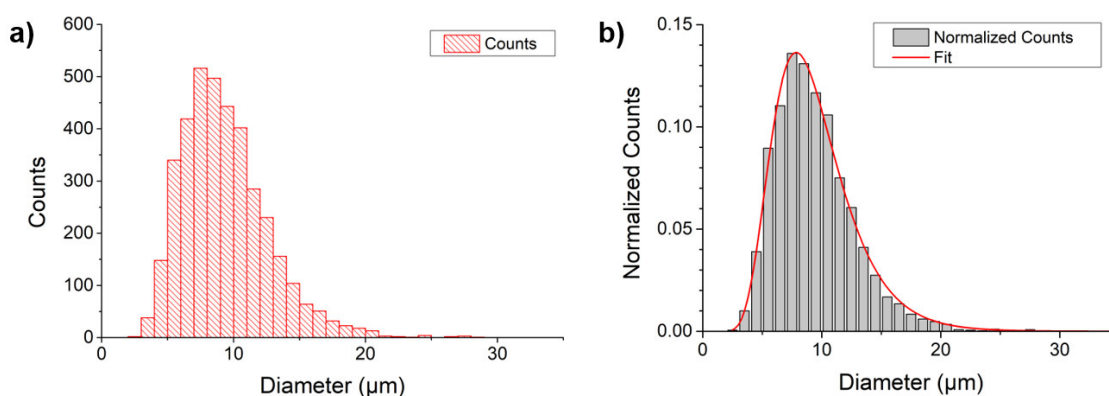


Figure 23: Schematics for the representation of collected data in a) a histogram and b) a normalized histogram with a fit

The mean values of the microstructure features and corresponding standard deviations were also calculated and plotted for the investigated cooling rate. This enables the comparison of the values for different holding temperatures.

Mean values, for example of the area fraction of α_p and the thickness of α_{GB} for one cooling rate, were determined by first calculating the mean value of each analyzed micrograph. Then, the mean value and standard deviation was calculated from the single mean values of each micrograph.

3.3.6 EBSD measurements

EBSD (electron backscattered diffraction) measurements were performed to investigate protuberances of α phase evolving from α_p particles along the β grain boundaries. Specimens for the EBDS characterization were first ground and polished as described in Table 7 and afterwards additionally vibro-polished for 24 h using an acidic suspension of Alumina. Subsequent EBSD measurement was conducted using a Tescan Mira3 SEM equipped with a Hikari Electron Backscattered Electrons camera. An area of 200 μm x 200 μm was measured using a step size of 0.2 μm . The data treatment was performed using the OIM Analysis[®] software. A confidence index

standardization was performed considering a grain with minimum size of 10 points and minimum misorientation angle of 12° . Finally, the neighbor confidence index correlation was utilized to re-index the data-points with confidence index lower than 0.75.

3.4 Analysis of dilatometer curves

Representation and analysis of the dilatometer curves of set 2 samples was also carried out using Origin[®] v9.0 [34]. Prior to the analysis, the ΔL -T-curves received from dilatometry were smoothed. Preparation and smoothing were performed in several steps:

- (1) Plotting ΔL (change in length) over T (temperature) for the temperature range of cooling
- (2) Evening out the jumps of the curve caused by instrumental error using addition/subtraction
- (3) Addition of initial sample length
- (4) Interpolation of the curve from 300°C to $930^\circ\text{C}/960^\circ\text{C}$ every 10°C
- (5) Smoothing with Adjacent-Averaging method (7 points per window)
- (6) Again, interpolation of the curve from 300°C to $930^\circ\text{C}/960^\circ\text{C}$ every 10°C
- (7) Differentiation of L-T-curve with respect to temperature
- (8) Smoothing using Savitzky-Golay method (7 points per window)
- (9) Dividing by the initial sample length to receive coefficient of thermal expansion (CTE)

After preparation, the CTE-T-curves were analyzed with regard to their peaks. Therefore, a baseline was set (Figure 24) and subtracted from the CTE-curve in a first step. Then, a multipeak fit with the inverse polynomial peak function (Equation 3) was performed (Figure 25). Two peaks were fitted. The first peak at higher temperatures representing the transformation of β phase in $\alpha_p + \alpha_{GB}$ phases and the second peak at lower temperatures representing the transformation in α_s phase. In the last step, the temperature at the peak maximum (T_T) and the area under the peak (A_T) was plotted against the cooling rate for both peaks. The peak maximum characterizes the highest rate of transformation for $\alpha_p + \alpha_{GB}$ and α_s . The area under the peak curve, i.e. the integral of the curve, is related to the energy released during the transformation

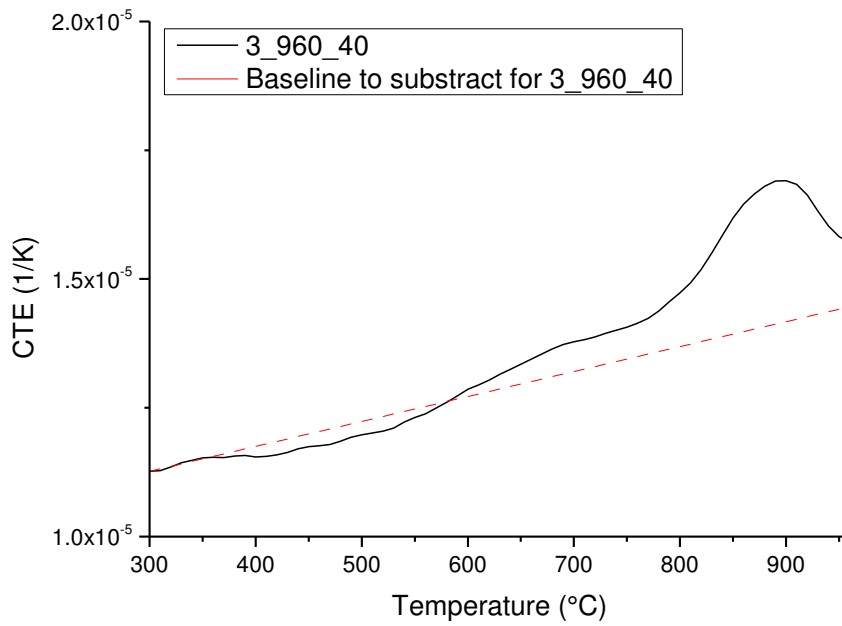


Figure 24: Obtaining the baseline for the CTE-T-curve (cooling) of sample 3_960_40

$$y = y_0 + \frac{A}{1 + A_1 \left(2 \frac{x - x_c}{w}\right)^2 + A_2 \left(2 \frac{x - x_c}{w}\right)^4 + A_3 \left(2 \frac{x - x_c}{w}\right)^6} \quad (\text{Equation 3})$$

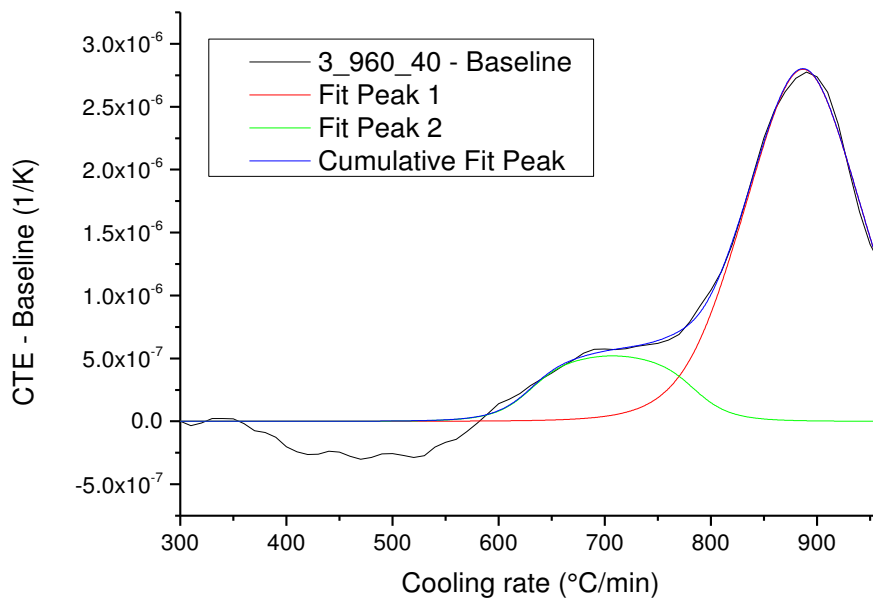


Figure 25: Fitting the peaks of the CTE-T-curve (cooling) of sample 3_960_40 after subtraction of the baseline

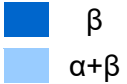






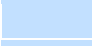


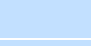

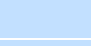
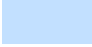
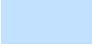
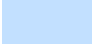
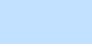
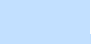
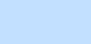
4 Results

In the following chapters, the results obtained from the conducted experiments are presented. Chapter 4.1 deals with the inhomogeneity of batch A. Subsequently, the microstructure of the heat treated samples as well as the microstructural changes during cooling are visualized in micrographs from samples of set 2 and set 3 captures by light optical microscopy and scanning electron microscopy. Lastly, the results from the image analysis and the analysis of dilatometer curves, also from set 2, are presented.

4.1 As received material of batch A

Microstructural analysis of set 1 using LOM showed, for some samples, a fully lamellar microstructure (Figure 26) without globular α_p phase even though a bimodal microstructure was expected after heat treatment under T_β of batch A. Table 8 shows which samples of set 1 showed a final microstructure referring to a heat treatment in the β field (dark blue), respectively a fully lamellar microstructure, and which showed a microstructure referring to a heat treatment in the $\alpha+\beta$ field (light blue), respectively a bimodal microstructure.

Table 8: Matrix showing the apparent heat treatment of the samples of set 1

		Cooling rate [°C/min]						
		300	100	40	30	10	2	
Holding temperature [°C]	980							β
	960							$\alpha+\beta$
	930							$\alpha+\beta$

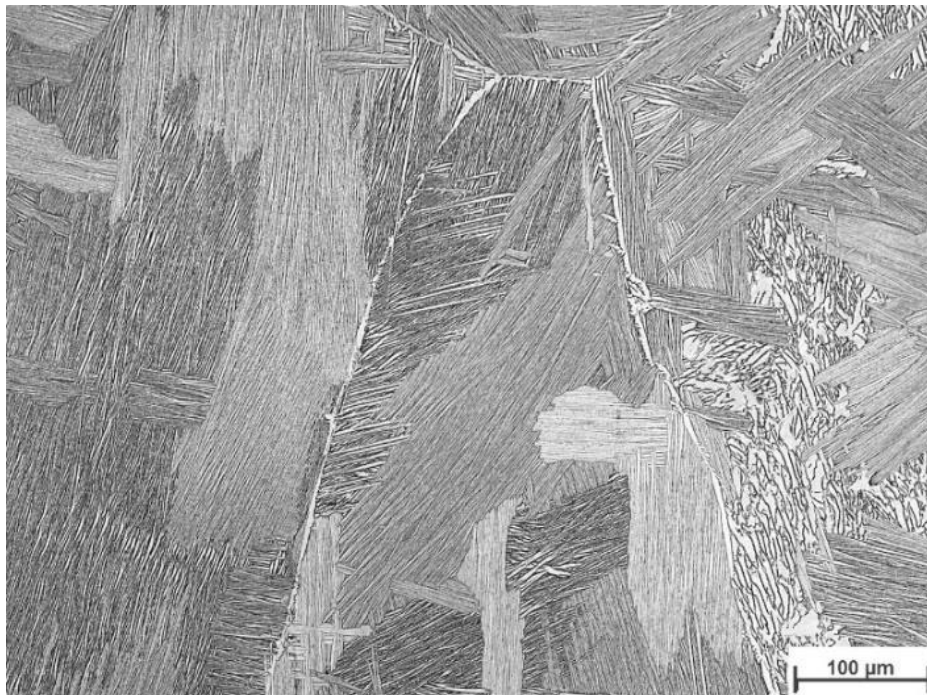


Figure 26: LOM image of sample 1_960_40 showing a fully lamellar microstructure

All samples heat treated at 930°C showed a bimodal microstructure, whereas all samples heat treated at 980°C showed a fully lamellar microstructure. Samples hold at 960°C revealed both, a microstructures corresponding to heat treatment in the $\alpha+\beta$ field for cooling rates of 300, 30 and 2°C/min, and a microstructure corresponding to heat treatment in the β field for cooling rates of 100, 40 and 10°C/min.

4.1.1 Microstructure of forged part before heat treatment

Due to forging, the material of batch A has regions with varying degrees of deformation and also regions that might be more susceptible to segregations. BSE-SEM investigations of the as-received forged part revealed slight differences in α_p content as well as some regions with different orientation, shape and size of particles.

Figure 27 shows micrographs from different regions in the forged part of batch A. As the α phase has a lower atomic weight than the β phase, the α phase appears dark and the β phase appears bright in BSE-mode. Micrographs c)-e) show elongated α_p particles. The orientation of the elongated particles corresponds well to the forging direction. Globular particles are found in other regions (Figure 27a, b, f). Slightly less content of α_p compared to the other micrographs is found in region corresponding to micrograph b).

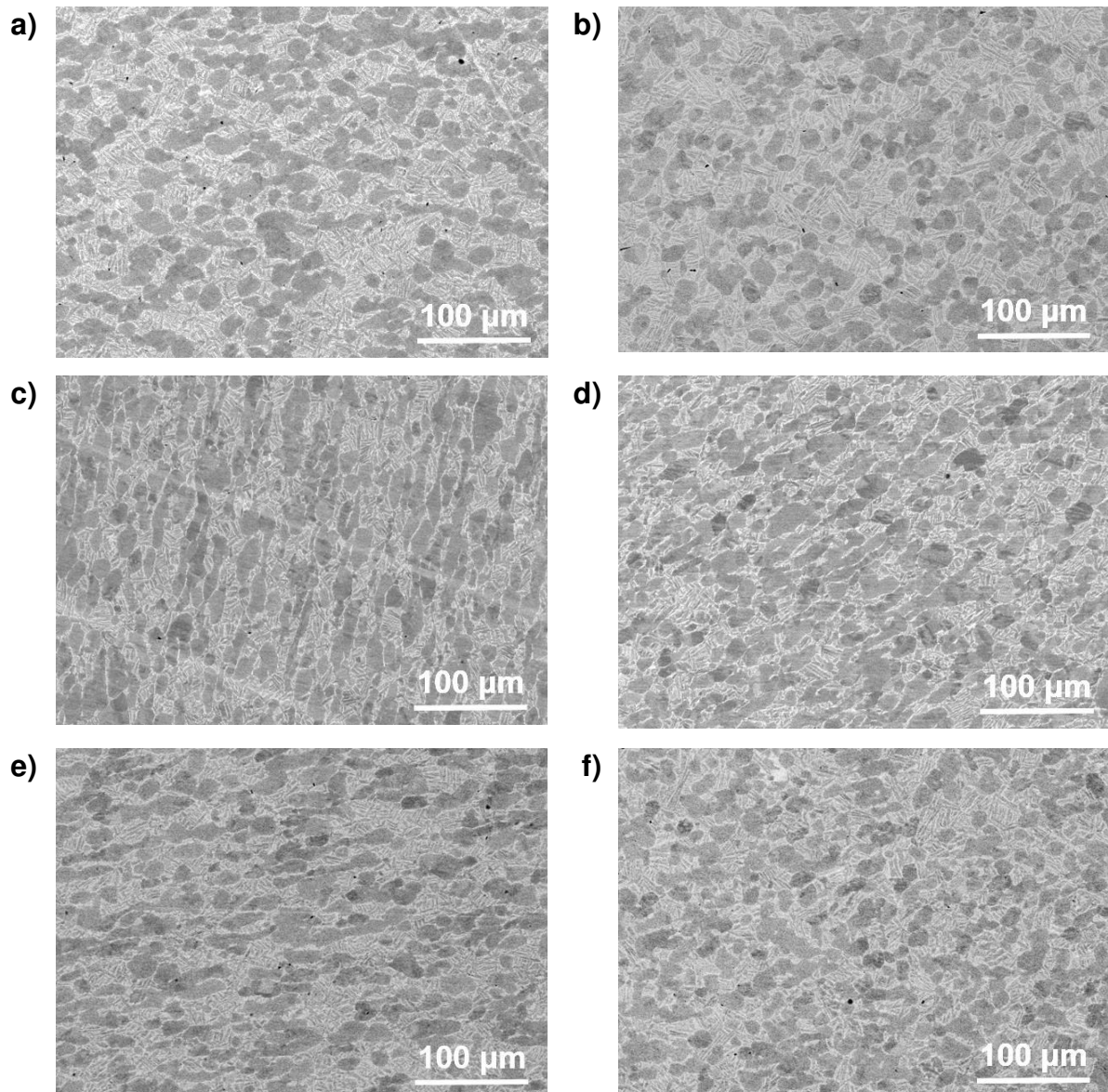


Figure 27: BSE-SEM micrographs showing microstructures in different regions of forged part of batch A

Figure 28 shows the element distribution measured with a line scan conducted in the frame of the EDX analysis of the forged part. The line scan started between two sample extraction holes and moved away from them. The oxygen content decreases qualitatively in this direction. Concurrently, the measured titanium content increases. Aluminum, vanadium and iron values stay in a constant range.

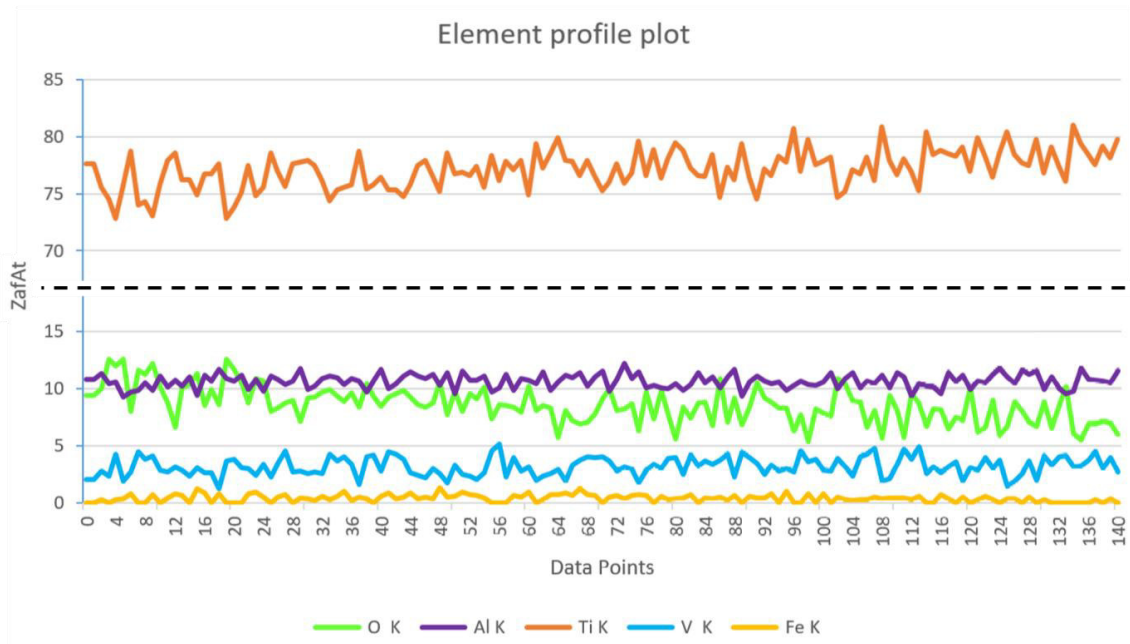


Figure 28: EDX-line scan of forged part showing a qualitative change in oxygen content

4.1.2 Microstructure of forged part after heat treatment

Micrographs of the forged part after heat treatment at 960°C for 10 min are shown in Figure 29. The heat treatment enhanced the differences in α_p content in comparison to Figure 27. Micrographs b) and d) reveal considerably lower fractions of α_p than micrograph a) and c).

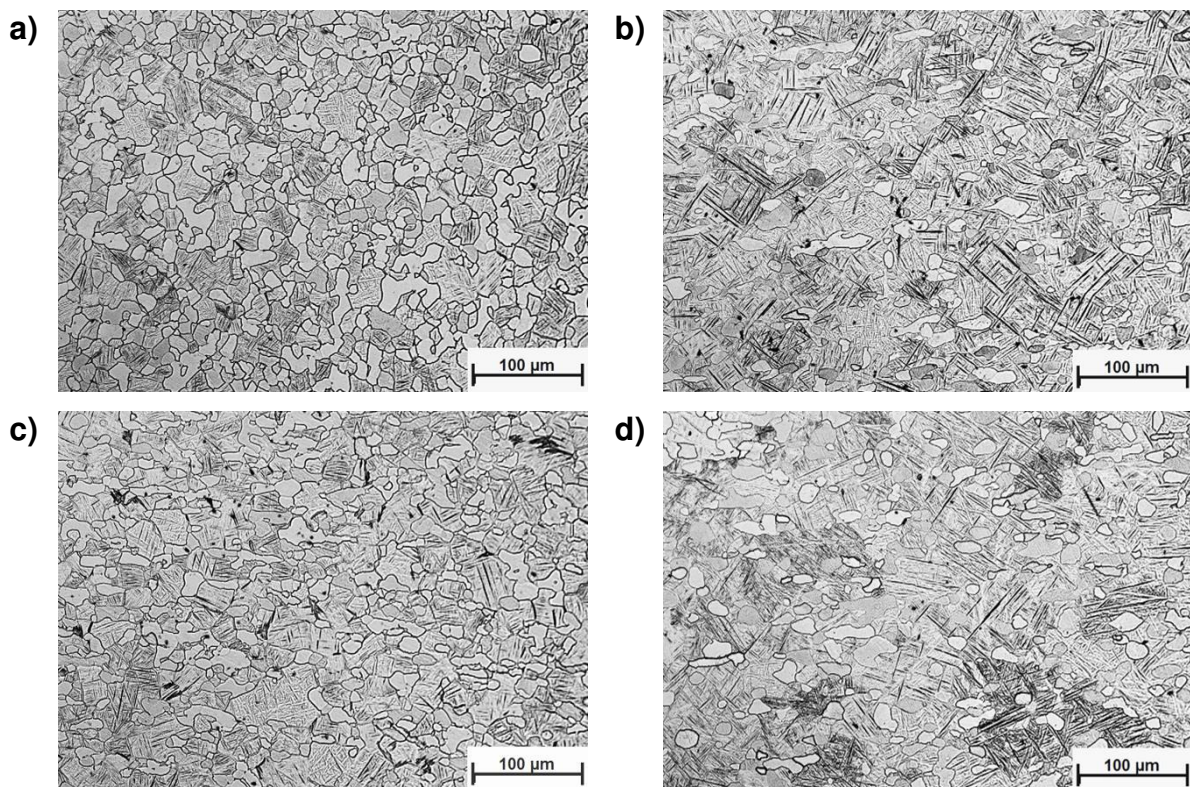


Figure 29: LOM micrographs showing microstructures in different regions of forged part of batch A after heat treatment for 10 min at 960°C and water quenching

4.2 Microstructural features

The micrographs presented in this chapter are obtained from samples of the material from batch B only. Figure 30 and Figure 31 show the microstructures of samples of set 2 after heat treatment. These samples are used for the quantification of α_p and α_{GB} . Figure 30 shows the evolution of α_p size for a holding temperature of 930°C for different cooling rates. The images show an increase in α_p size and fraction for decreasing cooling rates. Figure 31 shows the same trend for a holding temperature of 960°C. When comparing the microstructures for both holding temperatures, the α_p size and fraction also increase for decreasing holding temperatures.

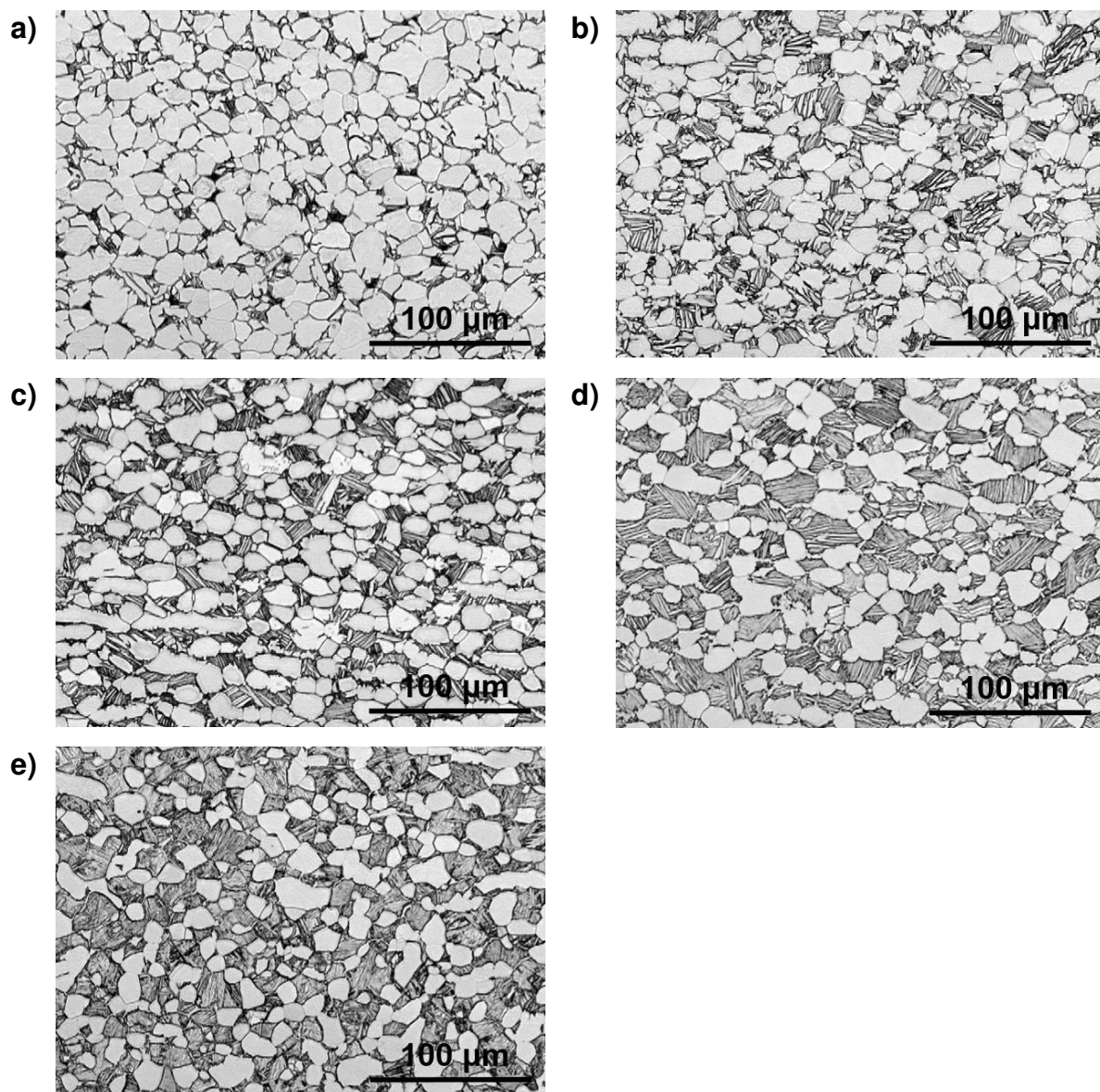


Figure 30: LOM micrographs of samples of set 2 (batch B) heated at 30°C/min, hold at 930°C for 60 min and cooled at a) 10°C/min, b) 30°C/min, c) 40°C/min, d) 100°C/min and e) 300°C/min

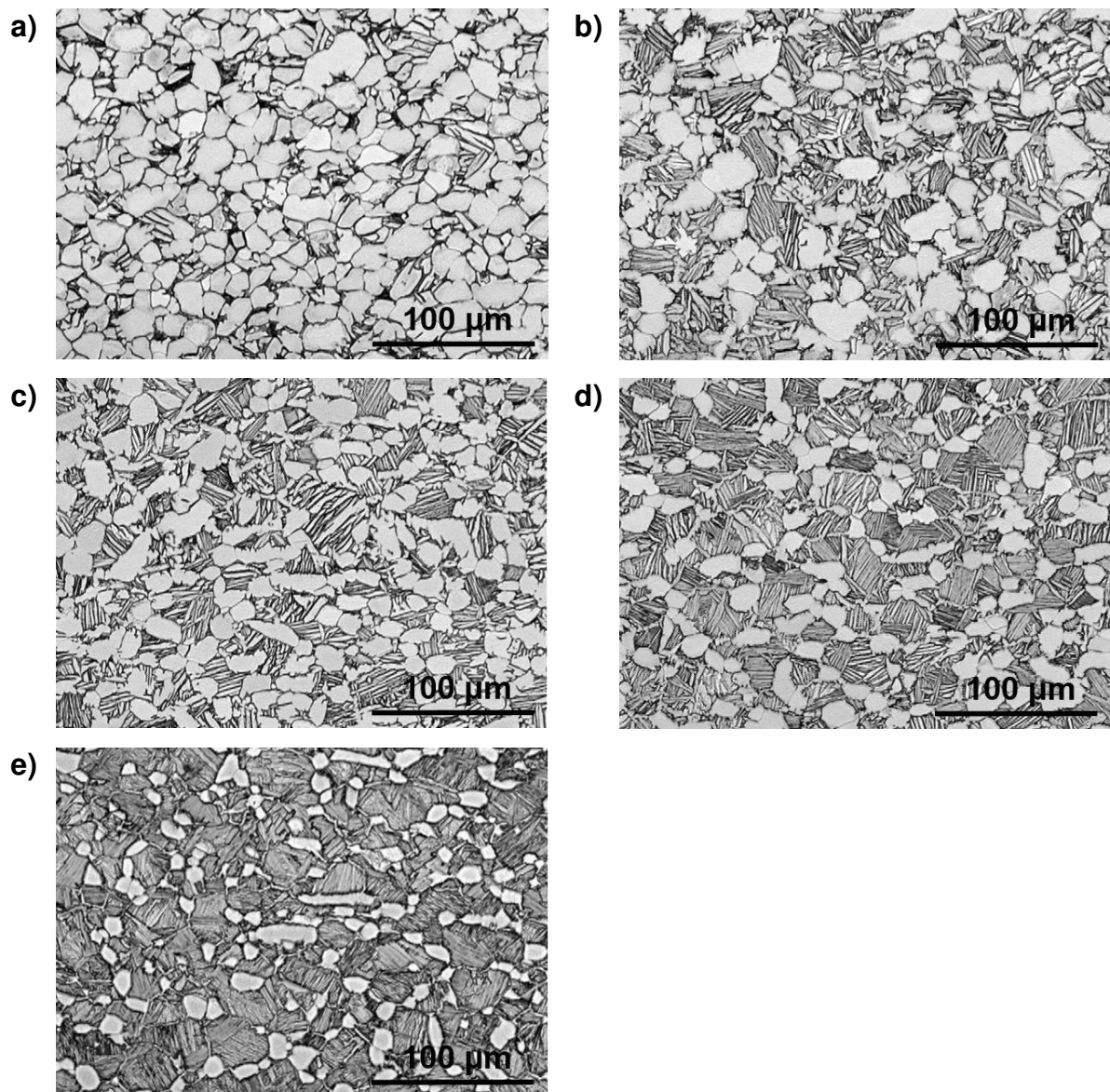


Figure 31: LOM micrographs of samples of set 2 (batch B) heated at 30°C/min, hold at 960°C for 60 min and cooled at a) 10°C/min, b) 30°C/min, c) 40°C/min, d) 100°C/min and e) 300°C/min

Figure 32 and Figure 33 show the same samples but highlighting the α_{GB} plates. For both holding temperatures, 930°C and 960°C, the thickness of the plates increases with decrease in the cooling rate. Unlike the size of α_p , the thickness of α_{GB} seems to be similar for both holding temperatures when comparing same cooling rates. With the decrease in cooling rate, the morphology of the α_{GB} plates becomes irregular and, therefore, harder to distinguish from the α_p particles.

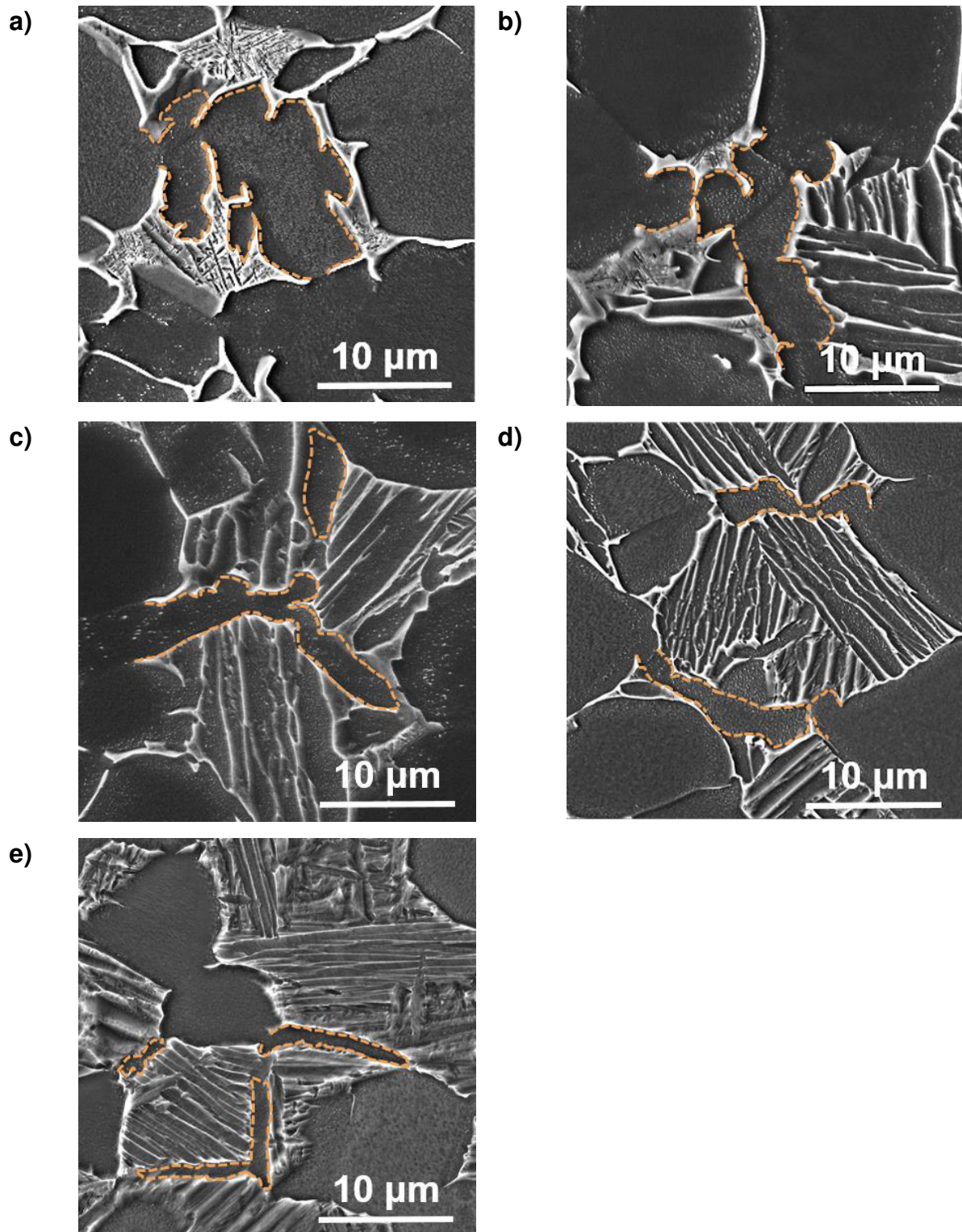


Figure 32: SE-SEM micrographs of samples of set 2 (batch B) heated at 30°C/min, hold at 930°C for 60 min and cooled at a) 10°C/min, b) 30°C/min, c) 40°C/min, d) 100°C/min and e) 300°C/min showing α_{GB} (orange) in detail

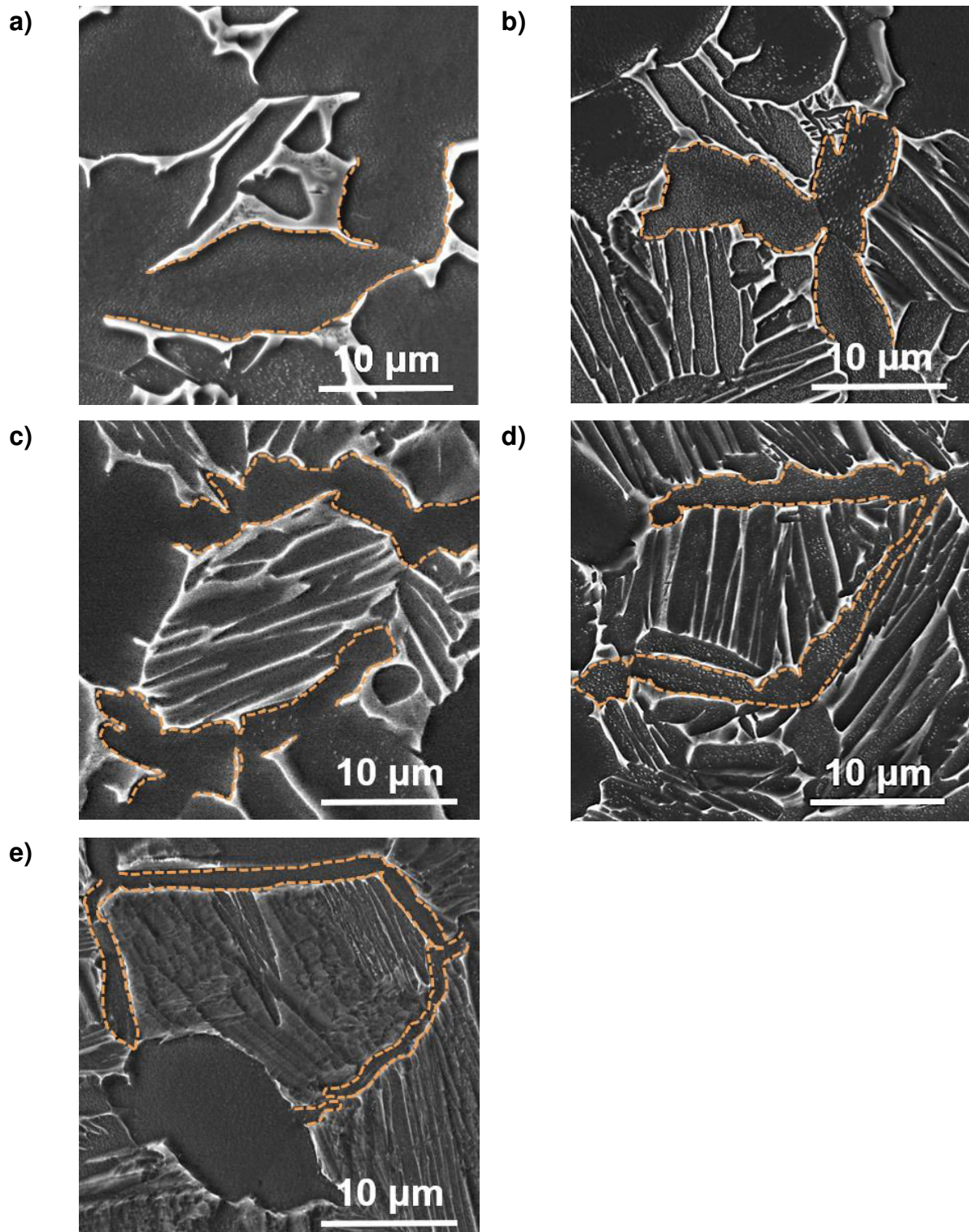


Figure 33: SE-SEM micrographs of samples of set 2 (batch B) heated at 30°C/min, hold at 960°C for 60 min and cooled at a) 10°C/min, b) 30°C/min, c) 40°C/min, d) 100°C/min and e) 300°C/min showing α_{GB} (orange) in detail

Set 3 consists of experiments with interrupted cooling. All samples were held at 960°C for 60 min. The microstructure shown in Figure 34 is representative of a sample quenched after the homogenization treatment. The α_p particles are small and separated.

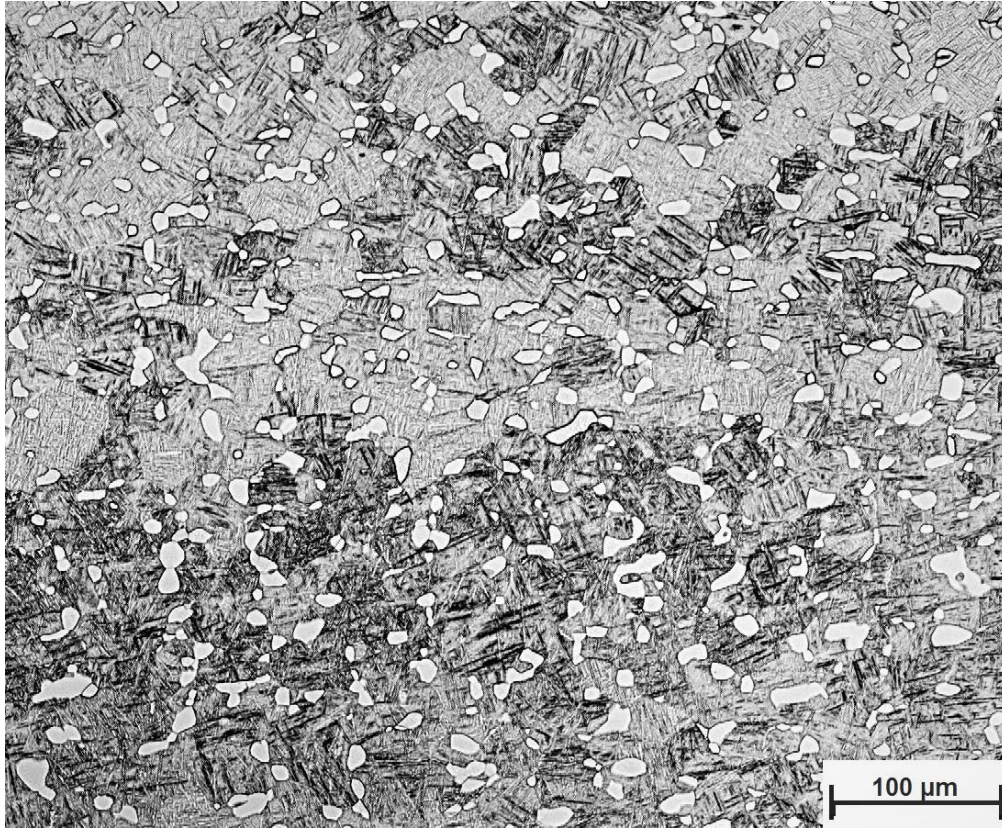


Figure 34: LOM micrograph of sample 4_960_ArQ960 heated at 30°C/min, hold at 960°C for 60 min and quenched with Argon

Figure 35 and Figure 36 show that the α_p particles grow during cooling from the annealing temperature. Simultaneously, the α_{GB} and α_s start to form. Figure 35 shows the microstructures for continuous cooling of 10°C/min for different interruption temperatures. The same is shown for the cooling rate of 100°C/min in Figure 36. For the cooling rate of 10°C/min, the α_p particles grow strongly between 960°C and 800°C, whereas the growth is limited for the higher cooling rate of 100°C/min. α_{GB} is visible for 100°C/min below 875°C, even though the magnification is not high. For 10°C/min, the α_{GB} plates are not defined. α_s is visible for quenching temperatures below 850°C and observed as small plates or dots, depending on their orientation. α_s is found between the globular particles for a cooling rate of 10°C/min and 100°C/min.

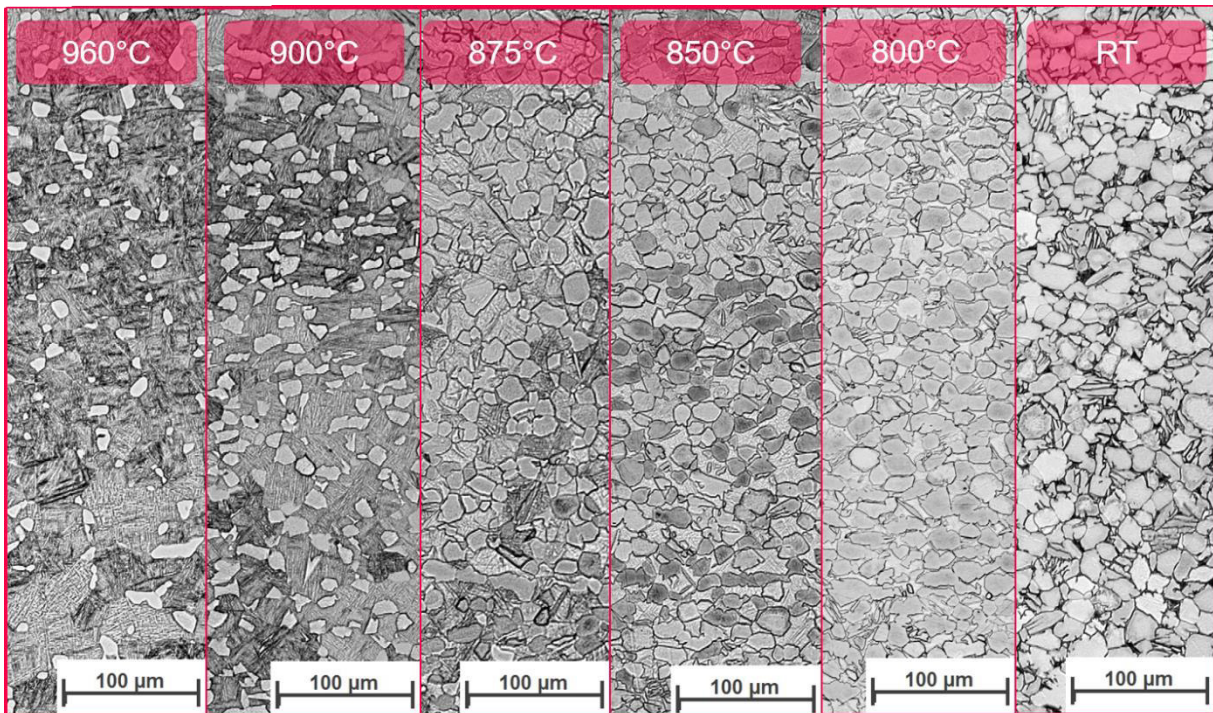


Figure 35: LOM micrographs of samples of set 3 (batch B) heated at 30°C/min, hold at 960°C for 60 min, cooled at 10°C/min and quenched at different temperatures showing formation and growth of α_p , α_{GB} and α_s

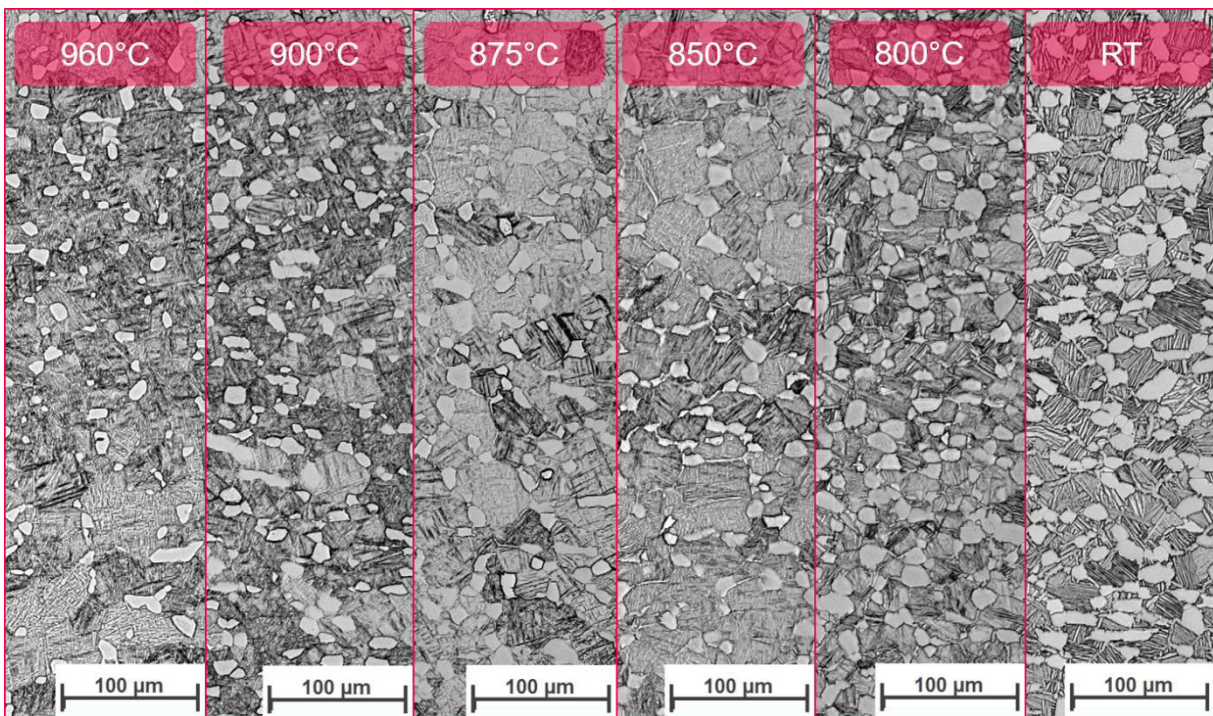


Figure 36: LOM micrographs of samples of set 3 (batch B) heated at 30°C/min, hold at 960°C for 60 min, cooled at 100°C/min and quenched at different temperatures showing formation and growth of α_p , α_{GB} and α_s

For a better understanding of the different growth mechanisms, additional micrographs were obtained using the SEM (Figure 37 and Figure 38). Figure 37 and Figure 38 show the progress of the growth of the different microstructural features at 900, 875, 850 and

800°C for cooling rate of 10°C/min and 100°C/min, respectively. Quenching at 900°C reveals that the allotriomorphic α_{GB} already started to grow at this temperature for both cooling rates. α_{GB} (indicated in pink) seems to grow preferentially from the globular α_p particles and along the prior β grain boundaries (indicated in yellow) as protuberances. Furthermore, a minor number of plates which seem to form at grain boundaries are visible (Figure 38b). For further cooling and quenching at 875°C, growth of α_{GB} continues. At 850°C, a difference in the growth of α_{GB} plates is observed when comparing the cooling rates of 10°C/min and 100°C/min. The α_{GB} plates are well-defined for 100°C/min, while for 10°C/min the plates are notably broadened. The plates seem to be part of the globular particles (see Figure 37c). Moreover, the formation of α_s (indicated in green) also occurs for both cooling rates at around 850°C. The α_s lamellas are thicker for 10°C/min compared to 100°C/min.

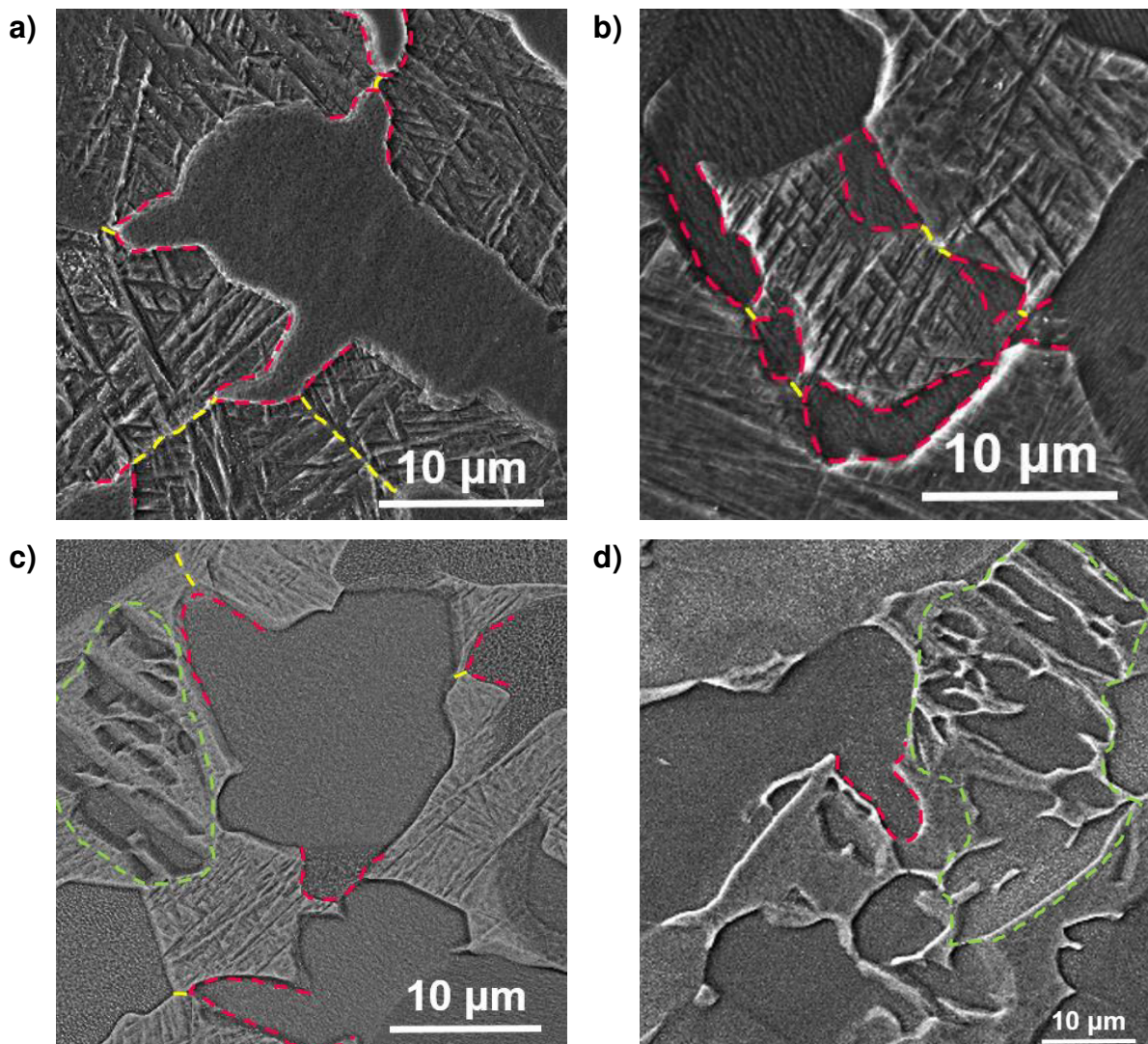


Figure 37: SEM micrographs of samples of set 3 (batch B) heated at 30°C/min, hold at 960°C for 60 min, cooled at 10°C/min and quenched at a) 900°C, b) 875°C, c) 850°C and d) 800°C showing details of formation and growth of α_{GB} (pink) along prior β grain boundaries (yellow) and α_s (green)

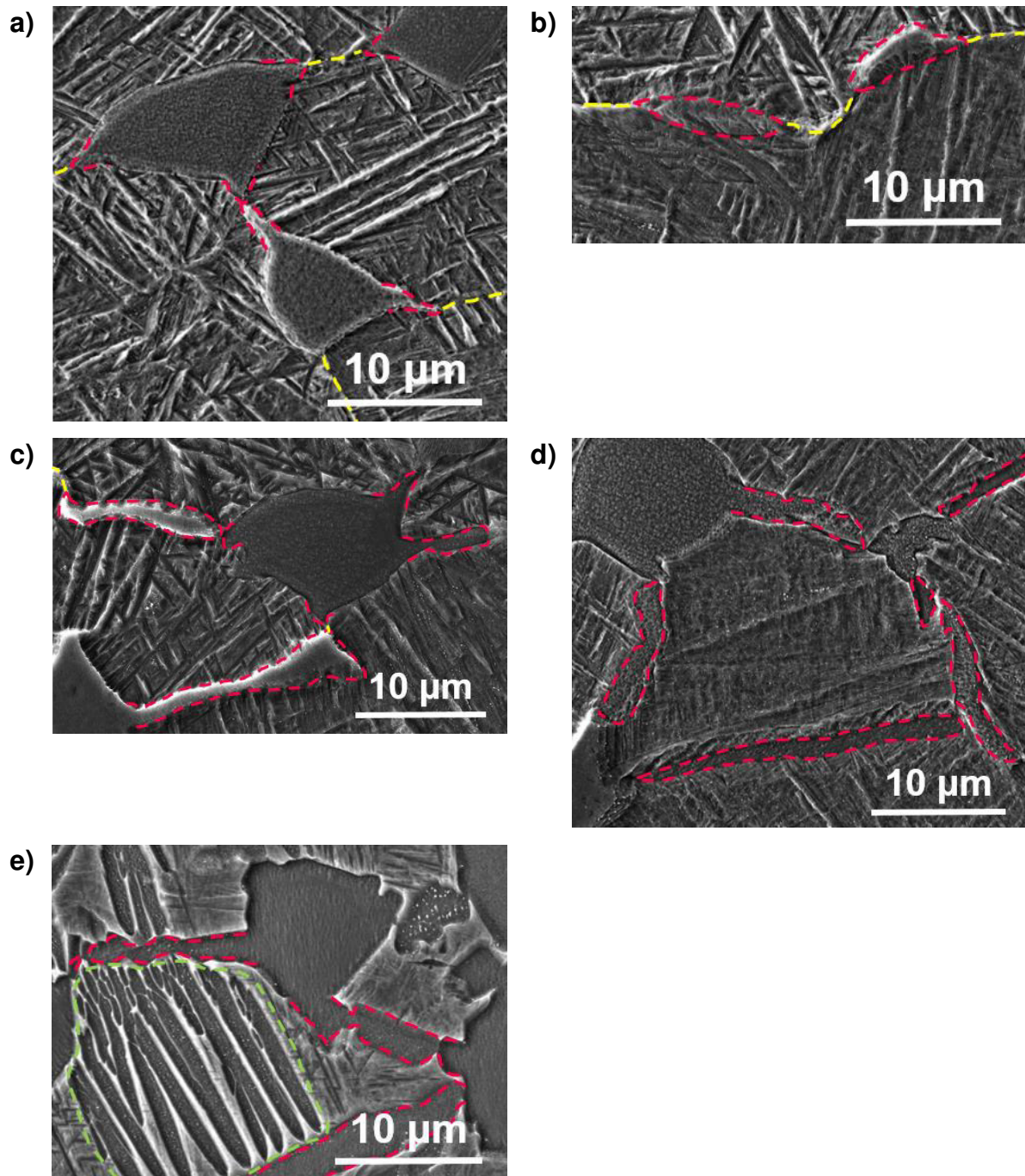


Figure 38: SEM micrographs of samples of set 3 (batch B) heated at 30°C/min, hold at 960°C for 60 min, cooled at 100°C/min and quenched at a), b) 900°C, c) 875°C, d) 850°C and e) 800°C showing details of formation and growth of α_{GB} (pink) along prior β grain boundaries (yellow) and α_s (green)

Figure 39 shows the microstructure of sample 4_1080_100_ArQ875. This sample was the only one from set 3 that was heat treated in the β field. Thus, the microstructure does not contain any globular α_p but α_{GB} was already formed at 875°C (see Figure 39b).

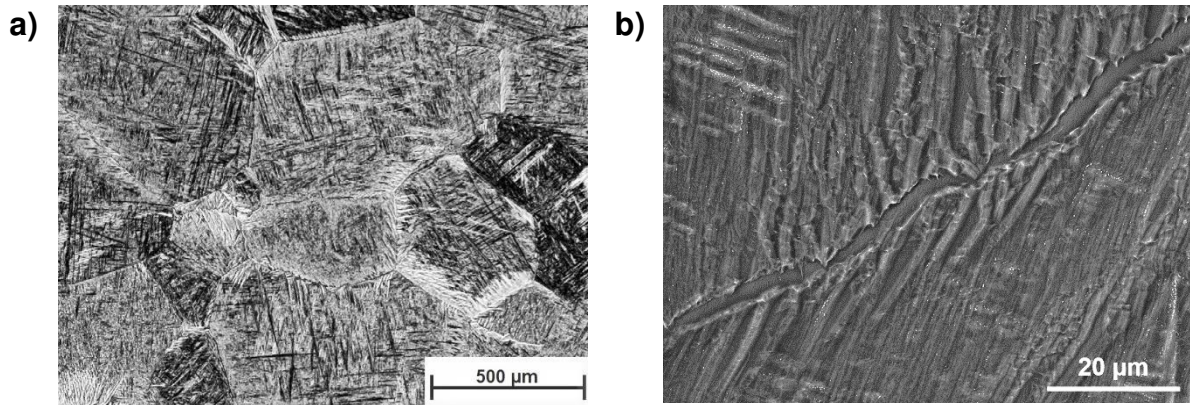


Figure 39: LOM (a) and SEM (b) micrographs of sample 4_1080_100_ArQ875 showing a) β grains and b) α_{GB} at the grain boundaries

The results obtained from the EBSD investigation of the protuberances of α_{GB} shown in Figure 37a and Figure 38a are presented in Figure 40. SEM micrographs and orientation maps are shown for quenching at 875°C and the cooling rates 10°C/min and 100°C/min. The orientation maps reveal that the protuberances exhibit the same crystallographic orientation as the α_p particles from which they evolve for both cooling rates.

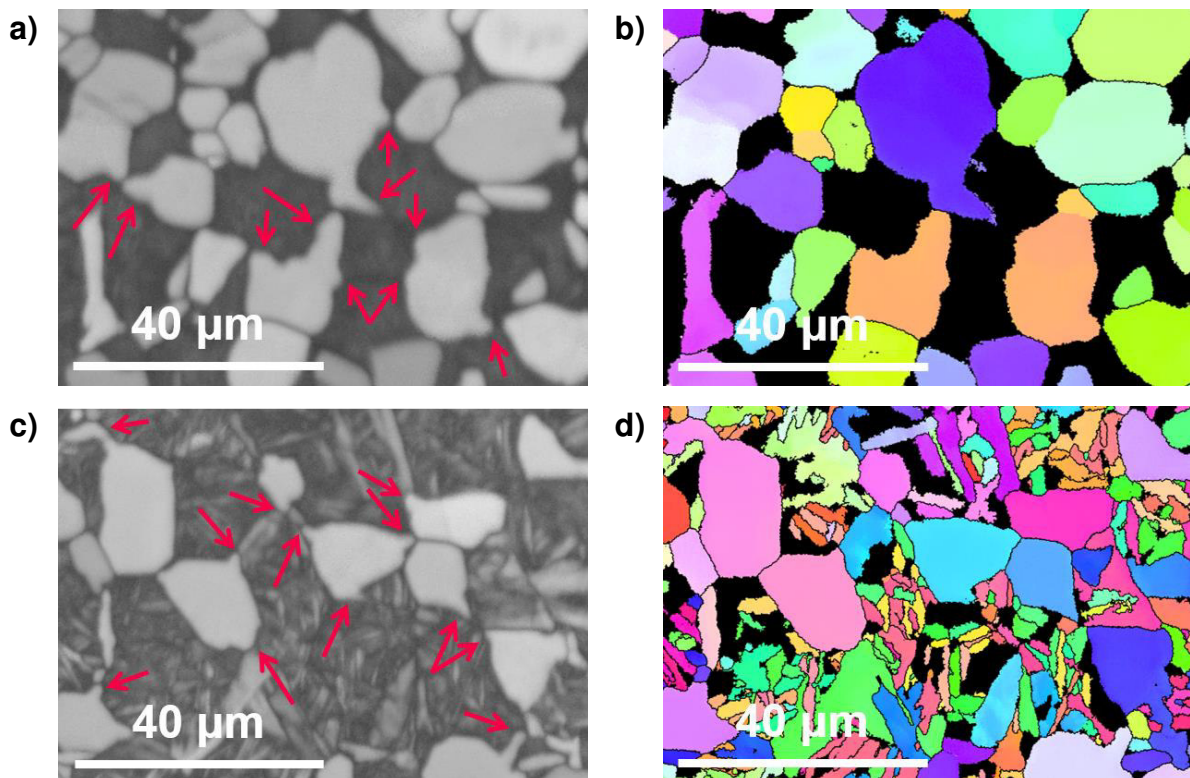


Figure 40: SEM micrographs (a,c) and corresponding EBSD orientation maps (b,d) for holding at 960°C and cooling at 10°C/min (a,b) and 100°C/min (c,d) followed by quenching at 875°C showing protuberances (red arrows) evolving from α_p

4.3 Data analysis of microstructural features

The graphs obtained from the quantitative evaluation (chapter 3.3.4) of the investigated samples of set 2 are presented in this chapter. Figure 41 shows the α_p diameter distributions for the cooling rates of 10, 30, 40, 100 and 300°C/min and the holding temperatures of 930°C and 960°C. The maximum value of the distribution shifts to larger diameters for decreasing cooling rates. Additionally, the distribution broadens with decrease in the cooling rate.

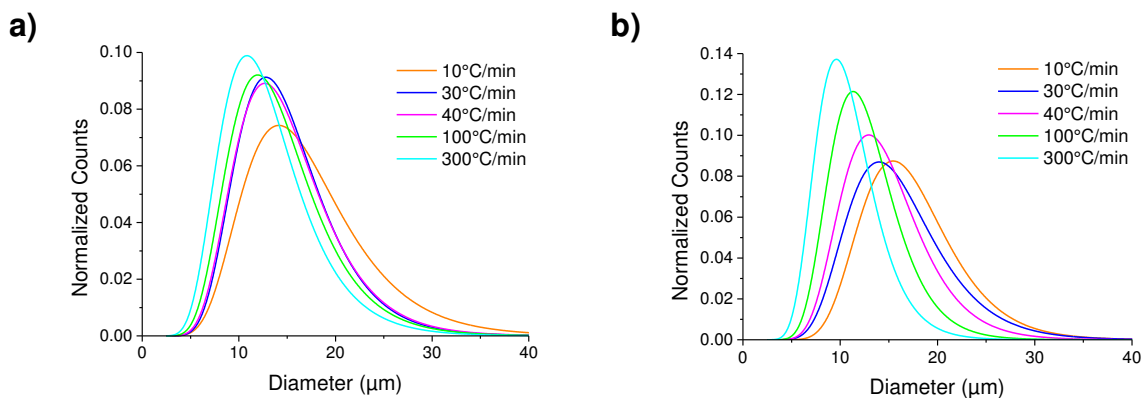


Figure 41: α_p diameter distributions for different cooling rates and holding temperatures of a) 930°C and b) 960°C

The graph in Figure 42 shows the dependence of the mean α_p diameter on the cooling rate for holding temperatures of 930°C and 960°C. The diameter increases for lower cooling rates. Furthermore, the mean diameter of the globular α_p is larger for lower holding temperatures and this difference becomes neglectable for low cooling rates.

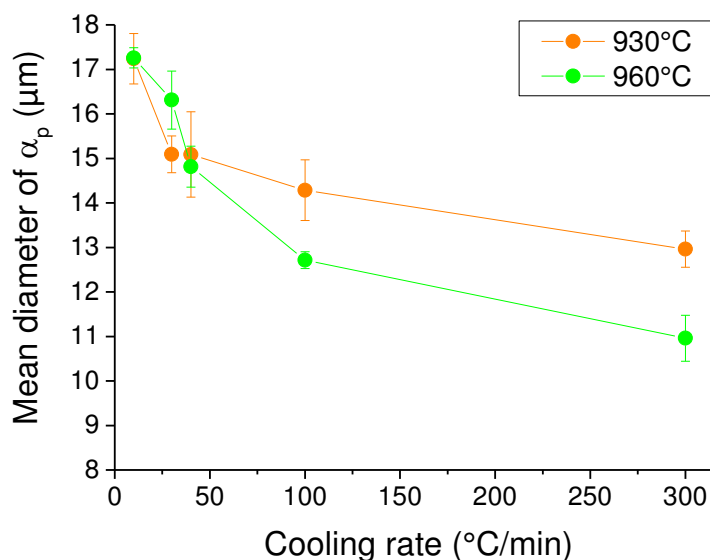


Figure 42: Mean α_p diameter for the investigated cooling rates for different holding temperatures

Figure 43 shows the evolution of the area fraction of α_p in dependence of the cooling rate. A decrease of the cooling rate causes an increase in the fraction of α_p . In comparison to the results from 960°C, the lower holding temperature of 930°C results in a higher α_p fraction.

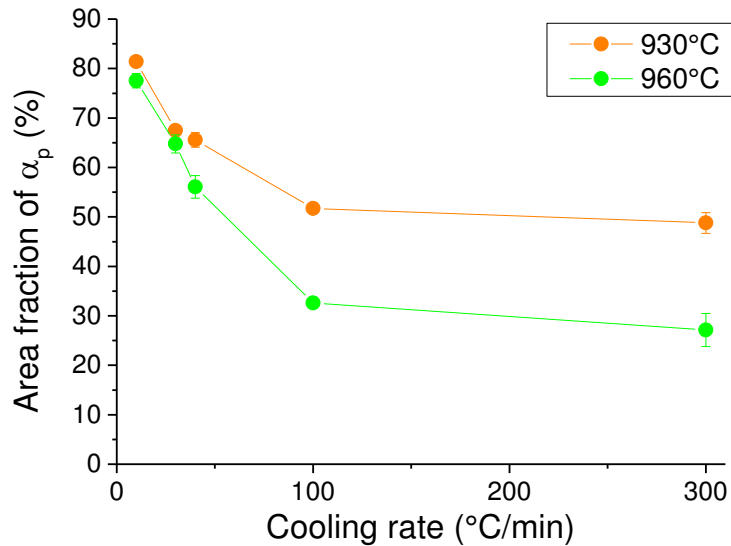


Figure 43: Area fraction of α_p for the investigated cooling rates for different holding temperatures

To describe the change of the shape of the α_p particles, the circularity as well as the aspect ratio are also shown as distributions for the different continuous cooling rates. Figure 44 exhibits the circularity distributions for holding temperatures of 930°C and 960°C, respectively. In both cases, the maxima of all distributions are between a circularity value of 0.7 to 0.9. Additionally, the circularity decreases with decrease in cooling rate.

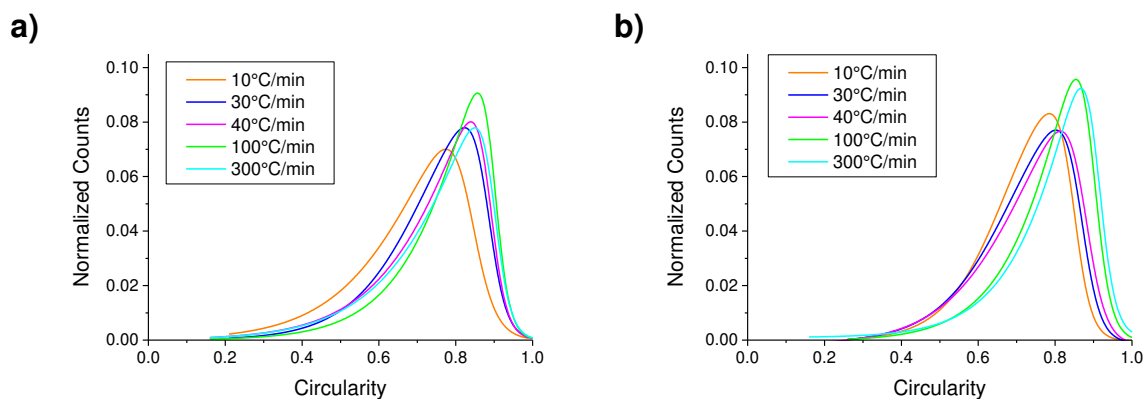


Figure 44: Circularity distributions of α_p for different cooling rates and holding temperatures of a) 930°C and b) 960°C

The distributions for the aspect ratio of α_p are displayed in Figure 45. Both graphs show a nearly constant maximum of the aspect ratio distribution and similar curves for all cooling rates and holding temperatures. The maxima of all distributions are around an aspect ratio value of 1.25.

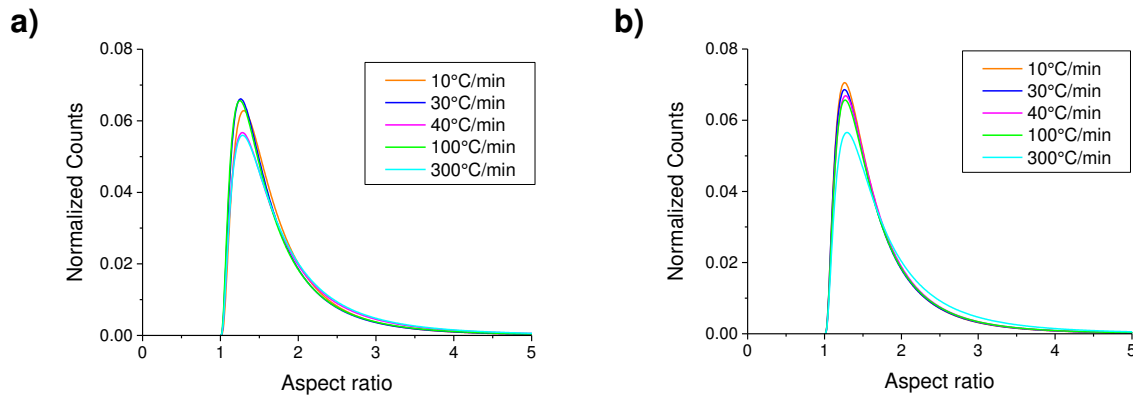


Figure 45: Aspect ratio distributions of α_p for different cooling rates and holding temperatures of a) 930°C and b) 960°C

Figure 46 shows the average area number density of α_p particles for both holding temperatures depending on the cooling rate. As there is no nucleation of α_p particles during cooling the number density is supposed to be one value for all cooling rates. The average value calculated from the mean values for each cooling rate is 3028 counts/mm² for 930°C and 2406 counts/mm² for 960°C. Thus, a higher number of α_p particles is found for the lower holding temperature.

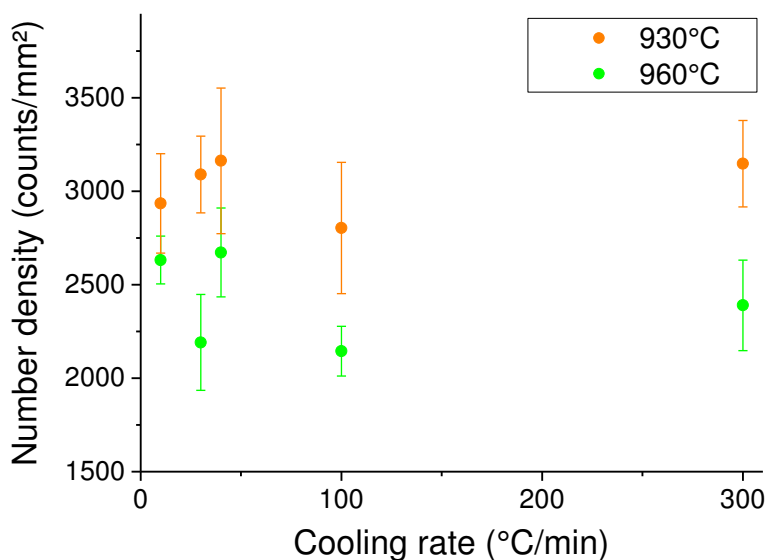


Figure 46: α_p number density for different cooling rates for different holding temperatures

In Figure 47 the thickness of α_{GB} plates plotted for the different cooling rates, and for both holding temperatures, is shown. The thickness increases with decrease of the cooling rate. Furthermore, the plate thickness is larger for the holding temperature of 960°C compared to 930°C. Plate thicknesses for a cooling rate of 10°C/min are not shown as the α_{GB} were not clearly distinguishable from the α_p .

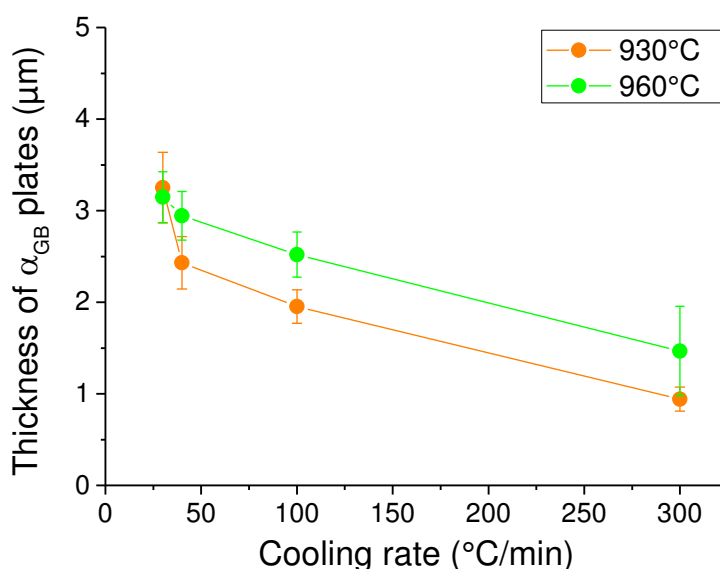


Figure 47: α_{GB} plate thickness for different cooling rates rate for different holding temperatures

4.4 Dilatometer curves

Dilatometer curves of samples of set 2 were also investigated to get further information about the transformation of β phase into primary and secondary α phase during continuous cooling. Figure 48 shows the CTE-T-curves for the conducted cooling rates for set 2 for the holding temperature of 930°C. Following the direction of cooling, the curves for the cooling rates 10, 30, 40 and 100°C/min start with a pronounced peak between 930°C and 800°C, for which the maxima are observed between 900°C and 850°C. The decrease of the CTE is diminished by a second, non-pronounced peak between 800°C and 600°C. During further cooling from 600°C, the CTE decreases constantly. The curve for a cooling rate of 300°C/min shows a different behavior. Between 930°C and ~875°C the CTE increases rapidly. Afterwards, the CTE decreases in a nearly constant manner.

The CTE-T-curves for a holding temperature of 960°C and cooling rates of 10, 30, 40 and 100°C/min (see Figure 49) show the same tendency as the curves for a holding temperature of 930°C and equal cooling rates. However, the second peak between 850°C and 600°C is easier to distinguish from the first peak as it is more pronounced

for the holding temperature of 960°C. The curve for the highest cooling rate of 300°C/min is also different compared to the others. Following the cooling direction, the curves show a first minimum at ~940°C and a second one at ~770°C. Between and for temperatures below ~690°C the curve shows a linear decrease of the CTE.

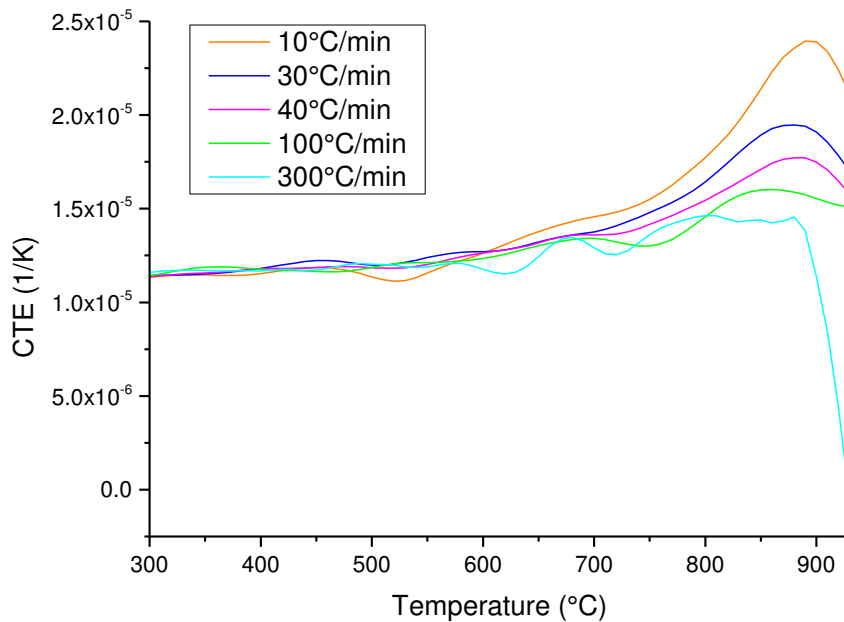


Figure 48: CTE-T-curves for different cooling rates for samples of set 2 hold at 930°C

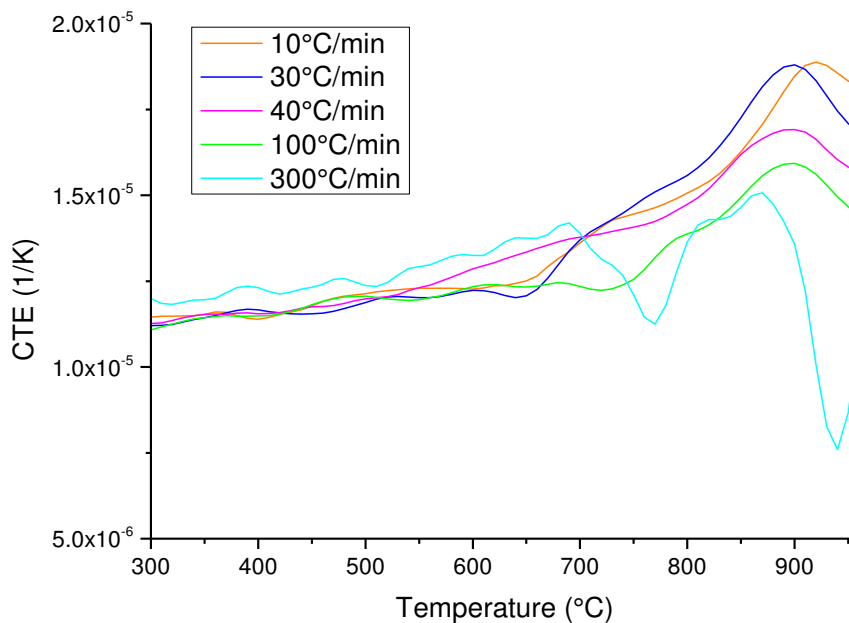


Figure 49: CTE-T-curves for different cooling rates for samples of set 2 hold at 960°C

4.5 Data analysis of dilatometer curves

The fitting of the peaks provided two parameters, which are both dependent on the holding temperature and cooling rate. The first one is the temperature of the maximum transformation rate (T_T), shown in Figure 50. The temperature is obtained for both the transformation of β phase into $\alpha_p + \alpha_{GB}$ and into α_s . The T_T is higher for $\alpha_p + \alpha_{GB}$ than for α_s . Furthermore, it is higher for the holding temperature of 960°C in comparison with 930°C. An exception is observed for the cooling rate 30°C/min. The temperatures of maximum transformation rate for $\alpha_p + \alpha_{GB}$ show a slight increase for decreasing cooling rates. A tendency for α_s is not visible, but the range of temperatures is between ~800°C and ~675°C.

Secondly, Figure 51 displays the holding temperature and cooling rate dependency of integrated area under the peak (A_T) for both $\alpha_p + \alpha_{GB}$ and α_s . The A_T is related the energy released during the transformation. Comparing the A_T for $\alpha_p + \alpha_{GB}$ and α_s transformation, it is lower for α_s . There is a slight tendency, that the area under the peak increases for decreasing cooling rates.

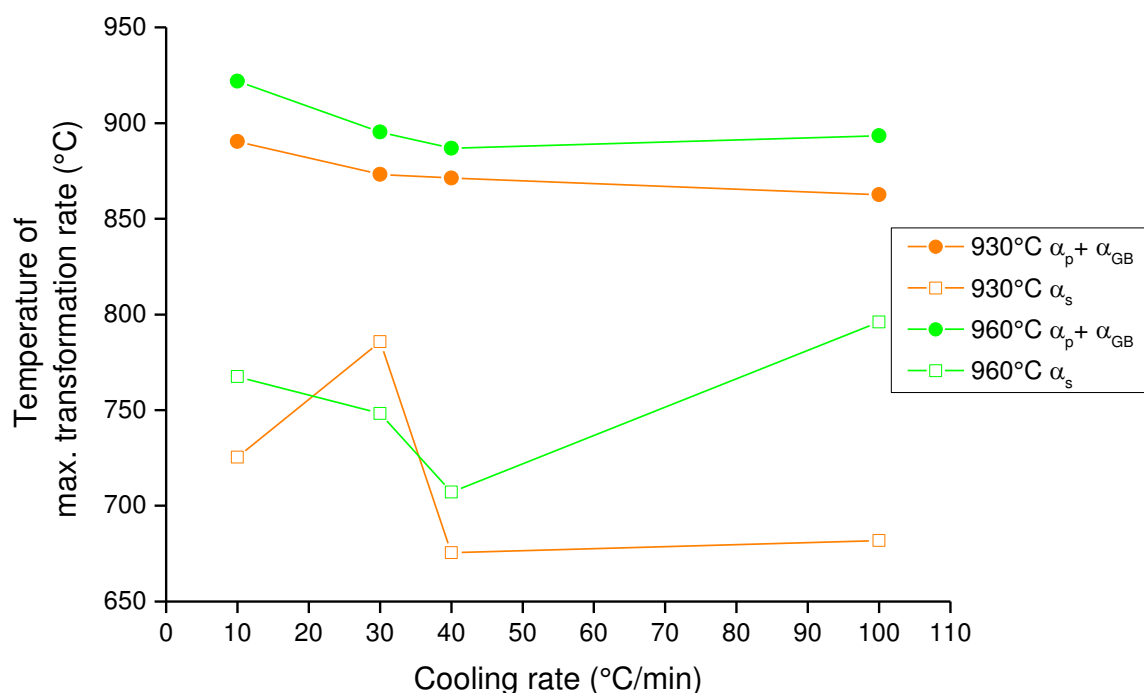


Figure 50: Temperature of maximum transformation rate of $\alpha_p + \alpha_{GB}$ and α_s plotted against the cooling rate for samples of set 2

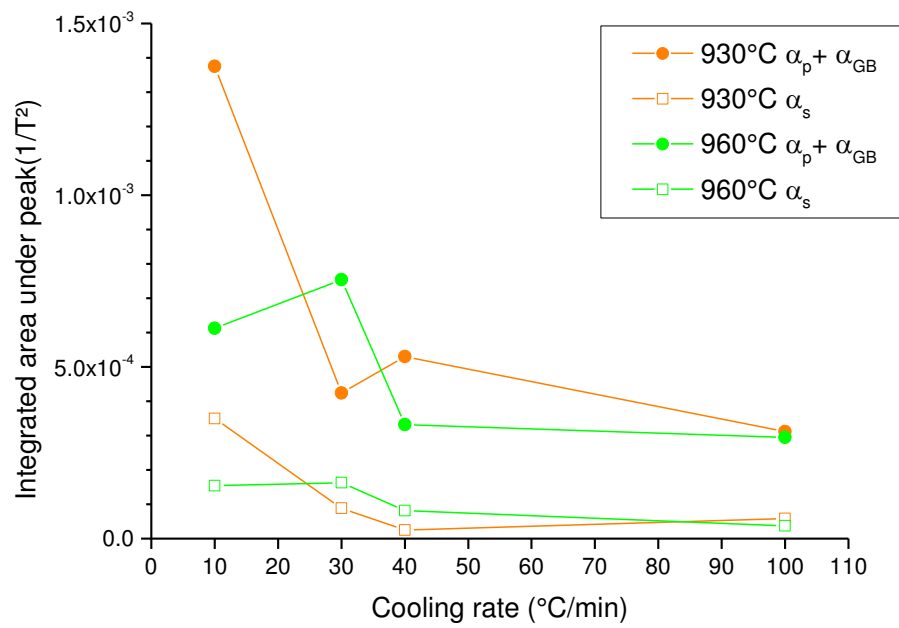


Figure 51: Integrated area under $\alpha_p + \alpha_{GB}$ and α_s peak depending on the cooling rate for holding temperatures of 930 $^{\circ}\text{C}$ and 960 $^{\circ}\text{C}$ for samples of set 2

5 Discussion

5.1 Behavior of Ti-6Al-4V during cooling

The results obtained from set 2 showed the dependence of the microstructure of the Ti-6Al-4V samples on the cooling rate and holding temperature used for different heat treatments. A quantitative analysis was only performed for the globular α_p phase and the α_{GB} phase forming at the β grain boundaries. Set 3 revealed the microstructure evolution dependent on the cooling rate. Further information about the transformation temperatures was received by the analysis of the dilatometer curves of set 2.

5.1.1 Dependence of final microstructure on cooling rate

The growth of α_p and α_{GB} in Ti-6Al-4V was investigated for two holding temperatures, 930°C and 960°C, and five cooling rates, 10, 30, 40, 100, 300°C/min. An increase in α_p fraction and mean diameter is observed for decreasing cooling rates. This change of α_p fraction was also investigated for Ti60 [21]. Both the α_p fraction and mean diameter show only a slight increase when changing the cooling rate from 300°C/min to 100°C/min. However, if the cooling rate is changed from 100°C/min to 10°C/min, fraction and size of α_p increase significantly. In this interval, the fraction increases by ~120% and the mean diameter by ~40%. The increase follows an exponential behavior and can be attributed to the significant increase in cooling time, respectively longer diffusion times, for cooling rates below 100°C/min.

Comparing the results for different holding temperatures, the fraction and mean diameter of α_p increases for lower holding temperatures. This fact is explained by the difference in particle size at the beginning of the cooling. When holding at 930°C, less α phase will dissolve as the equilibrium volume fraction for this phase is higher than for heat treatment at 960°C. Thus, the particle size at the start of cooling is already bigger. The resulting difference is clearly visible for the mean diameter and fraction of α_p at 300°C/min. Moreover, this difference becomes smaller for decreasing cooling rates which can also be attributed to longer times for diffusional growth for decreased cooling rates.

Independent of the holding temperature, the variations in distributions of diameter, circularity and aspect ratio for the globular α_p particles show the similar tendencies. The peak of the α_p diameter distribution shifts to higher value and the distribution broadens for decreasing cooling rates indicating that the growth of α_p is increased for lower cooling rates. Considering the shape of the particles, the peak values of the

circularity distributions range from 0.7 to 0.9 while the circularity decreases for decreasing cooling rates. In combination with the constant aspect ratio of ~ 1.25 , it can be approximated that the particles have a circular shape and become more irregular for slower cooling.

The number density of α_p particles shows big deviations but can be assumed to be constant for all the cooling rates. Moreover, the average number density is lower for the higher holding temperature of 960°C . This can be explained by a higher dissolution of α_p particles at higher holding temperatures.

Investigations revealed an increase in thickness of α_{GB} plates for decreasing cooling rates [12]. Furthermore, the plates are thicker for higher holding temperatures, which is opposing the bigger α_p size for lower holding temperatures. In contrast to the α_p particles, the α_{GB} seem to dissolve at both holding temperatures. Therefore, the α_{GB} plates have more time to grow when cooling from 960°C . This is supported by the fact, that the difference in plate thickness is nearly constant for cooling rates of 300, 100 and $40^\circ\text{C}/\text{min}$. At lower cooling rates, the morphology of the α_{GB} plates becomes irregular and, therefore, harder to distinguish from the α_p particles. Thus, no values for the α_{GB} plate thickness could be obtained for $10^\circ\text{C}/\text{min}$. The problems with distinguishing could also explain the increase for $30^\circ\text{C}/\text{min}$ at 930°C . Neglecting this value, the α_p thickness would show a nearly linear increase for both holding temperatures.

5.1.2 Sequence of formation and growth

The sequence of formation and growth of α_p and α_{GB} was observed for the cooling rates of $10^\circ\text{C}/\text{min}$ and $100^\circ\text{C}/\text{min}$. Firstly, sample 3_960_ArQ960 (Figure 34) was investigated to observe the microstructure after the homogenization treatment at 960°C and at the beginning of cooling. The micrograph revealed that the α_s and α_{GB} completely dissolved and the α_p shrank noticeably in comparison with the initial microstructure of batch B (Figure 13). The globular α_p particles are predominantly separated.

Quenching at 900°C revealed growth of α_p for cooling at $10^\circ\text{C}/\text{min}$ and $100^\circ\text{C}/\text{min}$. Moreover, the particles are still separated. Protuberances evolving from the α_p particles and growing along the β grain boundaries were found for both cooling rates $10^\circ\text{C}/\text{min}$ and $100^\circ\text{C}/\text{min}$. The EBSD investigation showed that the protuberances have the same crystallographic orientation as the α_p particles from which they start to grow. This agrees with investigations of Gao et al. [21] for Ti60. Cooling at $100^\circ\text{C}/\text{min}$ caused also

sporadic formation of α phase at the β grain boundaries (Figure 38b). Both features, the protuberances and the small particles forming at the grain boundaries are identified as α_{GB} .

In contrast to quenching at 900°C, quenching at 875°C showed already significant growth of the α_p particles for cooling at 10°C/min so that the particles start to be visibly connected. The α_p growth rate increased compared to the temperature interval between 960°C to 900°C. Only rare α_{GB} plates were observed. On the contrary, the α_p particles did not grow noticeably but large amount of α_{GB} plates were visible at 875°C for the cooling rate of 100°C/min. The β grain boundaries were partly or fully covered with α_{GB} plates. This implies that the α_{GB} growth rate could be increased for cooling at 100°C/min compared to 10°C/min. Then, the α_{GB} particles nucleated along the β grain boundaries would also exhibit a faster growth and cover the grain boundary. The thickness of these plates would also be thicker for 100°C/min compared to 10°C/min, which is not the case.

At 850°C, the slower growth of α_p was observed indicating a decrease in α_p growth rate for 10°C/min. Moreover, the particles are agglomerated. Only sporadic α_{GB} plates were visible at 850°C for the cooling rate of 10°C/min. This agrees with observations of [12] and [13]. Nevertheless, the reason for this seems not to be a lack of formation of α_{GB} plates as protuberances formed at 900°C. In fact, the growth of the observed protuberances competes with the growth of the α_p particles that showed to be extensive for a cooling rate of 10°C/min. For 100°C/min, the growth appears to follow opposite behavior. The growth of α_p was slower and the visible connectivity between particles was notably low. On the other hand, distinctive α_{GB} plates were formed and grew along the grain boundaries, in agreement with the literature [12]. Between 875°C and 850°C also α_s started to form for both cooling rates.

Cooling to 800°C caused growth of α_s . The lamellas of α_s were thicker for cooling rate of 10°C/min. But for 100°C/min a higher amount of α_s was formed indicating a higher nucleation rate. In general, when quenching at 800°C more β phase transformed into α phase for a cooling rate of 10°C/min explainable by the longer time for diffusional growth.

The analysis of the dilatometer curves (Figure 50 and Figure 51) showed that the T_T rate for the $\alpha_p + \alpha_{GB}$ is slightly higher for 10°C/min compared to 100°C/min. Considering that this value takes into account the transformation of β phase in α_p and in α_{GB} , a change in the temperature can be caused by both phases. As α_p shows an extensive

growth at 10°C/min, thus, the T_T may be more influenced by the α_p transformation instead of the α_{GB} transformation. The opposite way is observed for cooling at 100°C/min since the growth of α_{GB} is more pronounced. This can explain the higher T_T for transformation of $\alpha_p + \alpha_{GB}$ for cooling at 10°C/min compared to 100°C/min. The bigger A_T observed for 10°C/min compared to 100°C/min also corresponds to the high amount of formed α_p phase.

5.2 Limitations of image analysis

Due to the similar contrast of α_p , α_{GB} and α_s phases in LOM and SEM micrographs, the marking of globular α_p particles had to be performed manually. Thus, the analysis was time-consuming and dependent on the person who is conducting the analysis.

A second problem evolved from the similar morphology of α_p and α_{GB} phases. The lower the cooling rate, the harder it is to distinguish between the α_p and α_{GB} phases. Thus, an error affecting mainly the α_p fraction is caused when α_{GB} is unintentionally marked instead of α_p .

Lastly, the thickness of the black line drawn around the α_p particles for marking caused an error. Due to limitations of the ImageJ routine, the line could not be thinner. The error was reduced by adding 1.62 μm to the results for the α_p diameter and by adding half of the area fraction covered by the lines to the α_p fraction. Nevertheless, a small error remains as the marking lines are sometimes shared by two or more particles. The error caused by the thickness of the black lines could have been reduced by using LOM micrographs with higher resolution which enable use of thinner lines because of smaller pixel sizes.

6 Summary & Conclusions

In the present work, the effect of cooling rate on the growth kinetics of globular α_p and allotriomorphic α_{GB} in Ti-6Al-4V with initial bimodal microstructure was investigated after heat treatment in the $\alpha+\beta$ phase field and during continuous cooling. Due to microstructural inhomogeneity observed in material of batch A, the tests for quantitative analysis of α_p and α_{GB} as well as for qualitative evaluation of the sequence of formation and growth during continuous cooling were performed with material of batch B. Figure 52 shows a graphic representation of the conclusions that can be drawn from the investigations of batch B:

- (1) The size of α_p particles increases with decrease of the cooling rate because of the extended growth time. In contrast, the α_p diameter decreases if the holding temperature is increased as the size at the beginning of cooling is decreased. Moreover, the size distribution broadens with decrease of the cooling rate and its maximum shifts to higher values indicating a growth for all particles for slower cooling. The area fraction of α_p decreases with increase of both cooling rate and holding temperature. This is also attributed to shorter cooling times and more dissolution of α_p particles during holding, if the cooling rate and the holding temperatures are increased.
- (2) As the cooling rate decreases and the holding temperature increases the α_{GB} plates show an increase in thickness explained by longer growth times. Furthermore, the plate morphology is difficult to be distinguished from the α_p particles at low cooling rates, which impeded an accurate analysis of phase fraction of α_p .
- (3) Similar mechanisms are observed for low and high cooling rates regarding the formation and growth of α phases at the beginning of the cooling. The α_p particles grow and protuberances with same crystallographic orientation, identified as α_{GB} phase, evolve from the particles and grow along the prior β grain boundaries. Furthermore, sporadic formation of small α_{GB} particles at the β grain boundaries is also observed.
- (4) Continuous cooling shows different behaviors for low and high cooling rates. For high cooling rates, less growth of α_p and formation of well-defined α_{GB} plates is observed. Low cooling rates show an increase in growth of α_p due to increased time for diffusional growth. The α_p grows faster compared to

the growth of α_{GB} . Thus, some α_{GB} protuberances are consumed by the fast growth of the parent α_p particles. Moreover, α_s starts to form at lower temperatures for both cooling rates. For lower cooling rates lower amount of α_s is formed but the α_s lamellas are thicker compared to higher cooling rates.

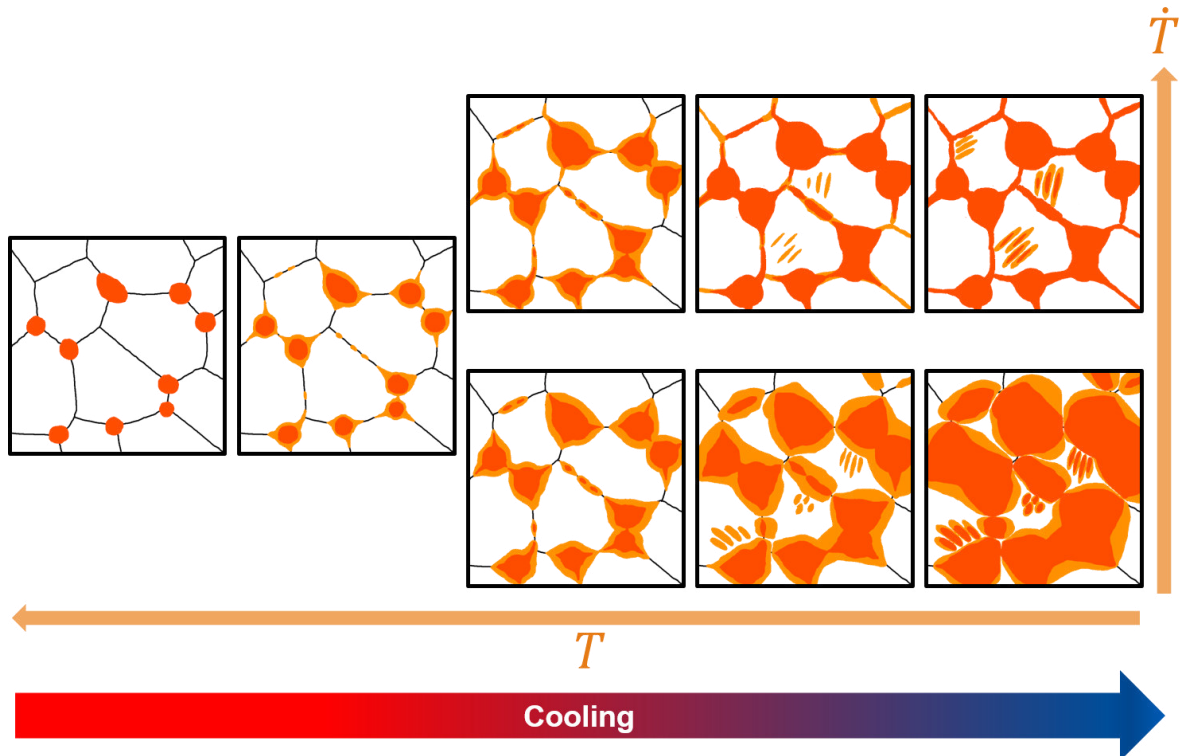


Figure 52: Schematic representation of the growth of α_p , α_{GB} and α_s during continuous cooling from a temperature in the $\alpha+\beta$ field for different cooling rates in Ti-6Al-4V

7 Outlook

The results obtained from the present work will be used for validation of a model depicting the coupled growth of circular particles of α_p and plates of α_{GB} as well as nucleation of α_s in Ti-6Al-4V and similar titanium alloys. Moreover, the results support the establishment of a model providing a diameter distribution instead of only mean values.

In addition, the established model is aimed to be used for simulation of hot deformation and phase transformation in a component manufactured in an industrial process. The linkage of all models enables the simulation of the entire thermo-mechanical processing of the component. As a result, the final microstructure of the part can be predicted and the required mechanical properties can be maintained.

References

- [1] F. H. Froes, *TITANIUM - Physical Metallurgy, Processing and Applications*. ASM International, 2015.
- [2] T. Choda, H. OYAMA, and S. MURAKAMI, "Technologies for process design of titanium alloy forging for aircraft parts," *Kobelco Technol. Rev.*, vol. 33, pp. 44–49, 2015.
- [3] G. Lütjering and J. C. Williams, *Titanium*. 2003.
- [4] C. Leyens and M. Peters, *Titanium and Titanium Alloys - Fundamentals and Applications*. Weinheim: WILEY-VCH Verlag GmbH & Co. KGaA, 2003.
- [5] S. Banerjee and P. Mukhopadhyay, "Phase Transformations - Examples from Titanium and Zirconium Alloys - Chapter 7 Diffusional Transformations," *Pergamon Mater. Ser.*, vol. 12, pp. 558–716, 2007.
- [6] G. Lütjering, "Influence of processing on microstructure and mechanical properties of (α + β) titanium alloys," *Mater. Sci. Eng.*, vol. 243, pp. 32–45, 1998.
- [7] A. Ducato, L. Fratini, M. La Cascia, and G. Mazzola, "An Automated Visual Inspection System for the Classification of the Phases of Ti-6Al-4V Titanium Alloy," in *CAIP 2013: Computer Analysis of Images and Patterns*, 2013, pp. 362–369.
- [8] R. Boyer, G. Welsch, and E. W. Collings, *Materials Properties Handbook: Titanium Alloys*. ASM International, 1994.
- [9] C. Veiga, J. P. Davim, and A. J. R. Loureiro, "Properties and applications of titanium alloys: A brief review," *Rev. Adv. Mater. Sci.*, vol. 32, pp. 133–148, 2012.
- [10] H. Fujii, K. Takahashi, and Y. Yamashita, "Application of titanium and its alloys for automobile parts," *Nippon Steel Tech. Rep.*, no. 88, pp. 70–75, 2003.
- [11] C. N. Elias, J. H. C. Lima, R. Valiev, and M. A. Meyers, "Biomedical applications of titanium and its alloys," *Jom*, vol. 60, no. 3, pp. 46–49, 2008.
- [12] R. Pederson, "Microstructure and Phase Transformation of Ti-6Al-4V," 2002.
- [13] S. L. Semiatin, S. L. Knisley, P. N. Fagin, F. Zhang, and D. R. Barker, "Microstructure evolution during alpha-beta heat treatment of Ti-6Al-4V.pdf," *Metall. Mater. Trans. A*, vol. 34A, pp. 2377–2380, 2003.
- [14] Z. Sun, X. Li, H. Wu, and H. Yang, "A unified growth model of the secondary grain boundary α phase in TA15 Ti-alloy," *J. Alloys Compd.*, vol. 689, pp. 693–701, 2016.
- [15] R. Banerjee, D. Bhattacharyya, P. C. Collins, G. B. Viswanathan, and H. L. Fraser, "Precipitation of grain boundary α in a laser deposited compositionally graded Ti-8Al-xV alloy - An orientation microscopy study," *Acta Mater.*, vol. 52, pp. 377–385, 2004.
- [16] R. Trivedi, "The role of interfacial free energy and interface kinetics during the growth of precipitate plates and needles," *Metall. Trans.*, vol. 1, pp. 921–927, 1970.
- [17] W. W. Mullins and R. F. Sekerka, "Morphological Stability of a Particle Growing by Diffusion or Heat Flow," *J. Appl. Phys.*, vol. 34, no. 2, pp. 323–329, 1963.

- [18] S. Malinov, P. Markovskiy, W. Sha, and Z. Guo, "Resistivity study and computer modelling of the isothermal transformation kinetics of Ti-6Al-4V and Ti-6Al-2Sn-4Zr-2Mo-0.08Si alloys," *J. Alloys Compd.*, vol. 314, no. 1–2, pp. 181–192, 2001.
- [19] F. J. Gil, M. P. Ginebra, J. M. Manero, and J. A. Planell, "Formation of α -Widmanstätten structure: Effects of grain size and cooling rate on the Widmanstätten morphologies and on the mechanical properties in Ti6Al4V alloy," *J. Alloys Compd.*, vol. 329, no. 1–2, pp. 142–152, 2001.
- [20] I. Katarov, S. Malinov, and W. Sha, "Finite element modeling of the morphology of β to α phase transformation in Ti-6Al-4V alloy," *Metall. Mater. Trans. A Phys. Metall. Mater. Sci.*, vol. 33, no. 4, pp. 1027–1040, 2002.
- [21] X. Gao, W. Zeng, S. Zhang, and Q. Wang, "A study of epitaxial growth behaviors of equiaxed alpha phase at different cooling rates in near alpha titanium alloy," *Acta Mater.*, vol. 122, pp. 298–309, 2017.
- [22] S. Zhu, H. Yang, L. G. Guo, and X. G. Fan, "Effect of cooling rate on microstructure evolution during α/β heat treatment of TA15 titanium alloy," *Mater. Charact.*, vol. 70, pp. 101–110, 2012.
- [23] M. Meng, X. G. Fan, H. Yang, L. G. Guo, M. Zhan, and P. F. Gao, "Precipitation of secondary alpha in competition with epitaxial growth of primary alpha in two-phase titanium alloys," *J. Alloys Compd.*, vol. 714, pp. 294–302, 2017.
- [24] M. Meng, H. Yang, X. G. Fan, S. L. Yan, A. M. Zhao, and S. Zhu, "On the modeling of diffusion-controlled growth of primary alpha in heat treatment of two-phase Ti-alloys," *J. Alloys Compd.*, vol. 691, pp. 67–80, 2017.
- [25] V. Raghavan, *Solid State Phase Transformations*. Delhi: PHI Learning Private Limited, 1987.
- [26] "JMatPro® Module: Titanium alloys." Sente Software Ltd., Version 10.2.
- [27] Matplus GmbH, "MATPLUS." [Online]. Available: <https://matplus.de/en/jmatpro/>. [Accessed: 30-Nov-2018].
- [28] P. Homporová, "Thermal history of alpha morphology in titanium alloy Ti-6Al-4V," Vienna University of Technology, 2011.
- [29] REOTEMP Instrument Corporation, "Thermocouple Info." [Online]. Available: <https://www.thermocoupleinfo.com/type-k-thermocouple.htm>. [Accessed: 30-Nov-2018].
- [30] J. I. Qazi, O. N. Senkov, J. Rahim, A. Genc, and F. H. S. A. M. Froes, "Phase transformations in Ti6Al4V- x H alloys Phase Transformations in Ti-6Al-4V – x H Alloys," *Metall. Mater. Trans. A*, vol. 32A, no. October, pp. 2453–2463, 2001.
- [31] The GIMP Team, "GIMP - GNU Image Manipulation Program." [Online]. Available: <https://www.gimp.org/>. [Accessed: 25-Nov-2018].
- [32] "ImageJ." [Online]. Available: <https://imagej.net/Welcome>. [Accessed: 25-Nov-2018].
- [33] T. Ferreira and W. Rasband, *ImageJ User Guide*. 2012.
- [34] "Origin®9.0." OriginLab Corporation.

List of figures

Figure 1: Schematic phase diagrams for Ti alloys showing the influence of alloying elements: neutral, α -stabilizing or β -stabilizing [4]	3
Figure 2: Classification of Ti alloys according to the three-dimensional β -isomorphous phase diagram [4]	4
Figure 3: LOM micrograph of a lamellar microstructure of Ti-6Al-4V showing α_s colonies and allotriomorphic α_{GB} along the grain boundaries	5
Figure 4: Different microstructures of $\alpha+\beta$ alloy Ti-6Al-4V: a) Fully lamellar, b) fully equiaxed, c) bimodal and d) martensitic structure	6
Figure 5: (Ti-6Al)-(V) phase diagram with straight line marking composition of Ti-6Al-4V [7]	8
Figure 6: Micrograph of TA15 showing different morphologies (flat, zig-zag and mixed) of α_{GB} [14]	10
Figure 7: SEM-BS micrographs showing the influence of Vanadium content on the morphology of α_{GB} in titanium alloy Ti-8Al-xV [15]	11
Figure 8: Micrographs illustrating the formation of α_s . Protuberances evolving from (A) α_p particles and (B) from α_{GB} layer as well as (C) nucleation within the β grain [13].	11
Figure 9: SEM-BSE micrograph showing rim- α phase in bimodal microstructure for a cooling rate of 90°C/min [21]	13
Figure 10: EBSD orientation map showing α_p particles and the extending phase (marked with black arrows) [21]	13
Figure 11: Effect of α_s formation on the volume fraction of α_p during continuous cooling (schematic) [13]	14
Figure 12: Light optical micrograph of the typical bimodal microstructure of the forged part from batch A	16
Figure 13: LOM micrograph showing the microstructure of batch B [28]	17
Figure 14: Welding of the thermocouple to the sample	19
Figure 15: Placing sample in the sample chamber	19
Figure 16: Representation of the temperature cycle utilized for the continuous cooling tests	20
Figure 17: Temperature cycle for the interrupted continuous cooling heat treatments	22

Figure 18: Schematic representation of the area investigated using light optical microscopy for the determination of the microstructure feature of the primary α phase	25
Figure 19: Methodology adopted for the quantitative analysis of α_p by a) light optical micrographs; marked globular α_p particles; and c) image analysis using ImageJ	27
Figure 20: Schematic representation of the shape evolution of a particle with change in circularity value	28
Figure 21: Schematics representation of minor and major axis of an ellipse that was fitted to a particle	28
Figure 22: SEM-SE micrographs of bimodal heat treated Ti-6Al-4V. a) The different morphologies (globular, lamellar, plates at grain boundaries) of α phase are shown; b) highlight of an allotriomorphic α phase along the grain boundary with the dashed lines used for the measurements of the thickness of α_{GB}	29
Figure 23: Schematics for the representation of collected data in a) a histogram and b) a normalized histogram with a fit	30
Figure 24: Obtaining the baseline for the CTE-T-curve (cooling) of sample 3_960_40	32
Figure 25: Fitting the peaks of the CTE-T-curve (cooling) of sample 3_960_40 after subtraction of the baseline.....	32
Figure 26: LOM image of sample 1_960_40 showing a fully lamellar microstructure	34
Figure 27: BSE-SEM micrographs showing microstructures in different regions of forged part of batch A	35
Figure 28: EDX-line scan of forged part showing a qualitative change in oxygen content	36
Figure 29: LOM micrographs showing microstructures in different regions of forged part of batch A after heat treatment for 10 min at 960°C and water quenching	36
Figure 30: LOM micrographs of samples of set 2 (batch B) heated at 30°C/min, hold at 930°C for 60 min and cooled at a) 10°C/min, b) 30°C/min, c) 40°C/min, d) 100°C/min and e) 300°C/min.....	37
Figure 31: LOM micrographs of samples of set 2 (batch B) heated at 30°C/min, hold at 960°C for 60 min and cooled at a) 10°C/min, b) 30°C/min, c) 40°C/min, d) 100°C/min and e) 300°C/min.....	38

Figure 32: SE-SEM micrographs of samples of set 2 (batch B) heated at 30°C/min, hold at 930°C for 60 min and cooled at a) 10°C/min, b) 30°C/min, c) 40°C/min, d) 100°C/min and e) 300°C/min showing α_{GB} (orange) in detail	39
Figure 33: SE-SEM micrographs of samples of set 2 (batch B) heated at 30°C/min, hold at 960°C for 60 min and cooled at a) 10°C/min, b) 30°C/min, c) 40°C/min, d) 100°C/min and e) 300°C/min showing α_{GB} (orange) in detail.....	40
Figure 34: LOM micrograph of sample 4_960_ArQ960 heated at 30°C/min, hold at 960°C for 60 min and quenched with Argon	41
Figure 35: LOM micrographs of samples of set 3 (batch B) heated at 30°C/min, hold at 960°C for 60 min, cooled at 10°C/min and quenched at different temperatures showing formation and growth of α_p , α_{GB} and α_s	42
Figure 36: LOM micrographs of samples of set 3 (batch B) heated at 30°C/min, hold at 960°C for 60 min, cooled at 100°C/min and quenched at different temperatures showing formation and growth of α_p , α_{GB} and α_s	42
Figure 37: SEM micrographs of samples of set 3 (batch B) heated at 30°C/min, hold at 960°C for 60 min, cooled at 10°C/min and quenched at a) 900°C, b) 875°C, c) 850°C and d) 800°C showing details of formation and growth of α_{GB} (pink) along prior β grain boundaries (yellow) and α_s (green)	43
Figure 38: SEM micrographs of samples of set 3 (batch B) heated at 30°C/min, hold at 960°C for 60 min, cooled at 100°C/min and quenched at a), b) 900°C, c) 875°C, d) 850°C and e) 800°C showing details of formation and growth of α_{GB} (pink) along prior β grain boundaries (yellow) and α_s (green)	44
Figure 39: LOM (a) and SEM (b) micrographs of sample 4_1080_100_ArQ875 showing a) β grains and b) α_{GB} at the grain boundaries	45
Figure 40: SEM micrographs (a,c) and corresponding EBSD orientation maps (b,d) for holding at 960°C and cooling at 10°C/min (a,b) and 100°C/min (c,d) followed by quenching at 875°C showing protuberances (red arrows) evolving from α_p	45
Figure 41: α_p diameter distributions for different cooling rates and holding temperatures of a) 930°C and b) 960°C	46
Figure 42: Mean α_p diameter for the investigated cooling rates for different holding temperatures	46
Figure 43: Area fraction of α_p for the investigated cooling rates for different holding temperatures	47

Figure 44: Circularity distributions of α_p for different cooling rates and holding temperatures of a) 930°C and b) 960°C	47
Figure 45: Aspect ratio distributions of α_p for different cooling rates and holding temperatures of a) 930°C and b) 960°C	48
Figure 46: α_p number density for different cooling rates for different holding temperatures	48
Figure 47: α_{GB} plate thickness for different cooling rates rate for different holding temperatures	49
Figure 48: CTE-T-curves for different cooling rates for samples of set 2 hold at 930°C	50
Figure 49: CTE-T-curves for different cooling rates for samples of set 2 hold at 960°C	50
Figure 50: Temperature of maximum transformation rate of $\alpha_p + \alpha_{GB}$ and α_s plotted against the cooling rate for samples of set 2	51
Figure 51: Integrated area under $\alpha_p + \alpha_{GB}$ and α_s peak depending on the cooling rate for holding temperatures of 930°C and 960°C for samples of set 2	52
Figure 52: Schematic representation of the growth of α_p , α_{GB} and α_s during continuous cooling from a temperature in the $\alpha + \beta$ field for different cooling rates in Ti-6Al-4V ..	58

List of tables

Table 1: Qualitative correlation between some basic microstructure features and mechanical properties for $\alpha + \beta$ titanium alloys [3]	8
Table 2: Typical mechanical properties of titanium alloy Ti-6Al-4V [4]	9
Table 3: Chemical composition of batch A [wt.%]	15
Table 4: Chemical composition of batch B [wt.%] [28]	16
Table 5: List of experiments and parameters for continuous cooling tests (set 1 & 2)	21
Table 6: List of experiments and parameters for the interrupted continuous cooling tests (set 3)	23
Table 7: Detailed steps and procedure for the metallographic preparation procedure of Ti-6Al-4V	24
Table 8: Matrix showing the apparent heat treatment of the samples of set 1	33

List of symbols and abbreviations

A_T	Integrated area under transformation peak
BSE	Backscattered electrons mode in scanning electron microscopy
EBSD	Electron backscattered diffraction
EDXS	Energy dispersive X-ray spectroscopy
LOM	Light optical microscope
OP-S	oxide polishing suspension
SE	Secondary electrons mode in scanning electron microscopy
SEM	Scanning electron microscope
Ti64, Ti-6Al-4V	Titanium alloy with 6 wt.% of Aluminum and 4 wt.% of Vanadium
T_T	Temperature of maximum transformation rate
T_β	Beta transus temperature
α_{GB}	Alpha phase at the grain boundaries
α_p	Globular primary alpha phase
α_s	Lamellar secondary alpha